

# Enhanced Grid-Following (E-GFL) Inverter: A Unified Control Framework for Stiff and Weak Grids

Alireza Askarian<sup>1</sup>, Member, IEEE, Jaesang Park<sup>2</sup>, Graduate Student Member, IEEE,  
and Srinivasa Salapaka<sup>3</sup>, Senior Member, IEEE

**Abstract**—This article presents an extensive framework focused on the control design, along with stability and performance analyses, of grid-following (GFL) inverters. It aims to ensure their effective operation under both stiff and weak grid conditions. The proposed framework leverages the coupled algebraic structure of the transmission line dynamics in the  $dq$  frame to express and then mitigate the effect of coupled dynamics on the GFL inverter's stability and performance. In addition, we simplify the coupled multi-input multi-output (MIMO) closed-loop system of the GFL into two separate single-input single-output (2-SISO) closed loops for easier analysis and control design. We present the stability, robust stability, and performance of the original GFL MIMO closed-loop system through our proposed 2-SISO closed-loop framework. This approach simplifies both the control design and its analysis. Our framework effectively achieves grid synchronization and active damping of filter resonance via feedback control. This eliminates the need for separate phase-locked loop and virtual impedance subsystems. We also utilize the Bode sensitivity integral to define the limits of GFL closed-loop stability margin and performance. These fundamental limits reveal the necessary tradeoffs between various performance goals, including reference tracking, closed-loop bandwidth, robust synchronization, and the ability to withstand grid disturbances. Finally, we demonstrate the merits of our proposed framework through detailed simulations and experiments. These showcase its effectiveness in handling challenging scenarios, such as asymmetric grid faults, low-voltage operation, and the balance between harmonic rejection and resonance suppression.

**Index Terms**—Active damping, asymmetrical fault, Bode sensitivity, control systems, grid-following (GFL) inverter, microgrid, multi-input multi-output (MIMO) systems, phase-locked loop (PLL), power system harmonics, robust stability, virtual impedance, virtual inertia, weak grid.

## I. INTRODUCTION

**I**N THE last two decades, there has been a significant effort to develop a decentralized power network that

Manuscript received 16 September 2023; revised 11 December 2023; accepted 3 January 2024. Date of publication 5 January 2024; date of current version 20 March 2024. This work was supported by the Advanced Research Projects Agency-Energy (ARPA-E) through the ARPA-E OPEN project titled “Rapidly Viable Sustained Grid” under Grant DE-AR0001016. Recommended for publication by Associate Editor B. Mirafzal. (Corresponding author: Alireza Askarian.)

The authors are with the Department of Mechanical Science and Engineering, University of Illinois at Urbana-Champaign, Urbana, IL 61801 USA (e-mail: askaria2@illinois.edu; jaesang4@illinois.edu; salapaka@illinois.edu).

Color versions of one or more figures in this article are available at <https://doi.org/10.1109/TPEL.2024.3350528>.

Digital Object Identifier 10.1109/TPEL.2024.3350528

enables the large-scale integration of distributed energy resources (DERs) [1]. This has led to the development of *microgrids*, where power subnetworks are formed to establish an autonomous grid or connect to the main power grid. Switching power systems, with their powerful digital processing capabilities and fast dynamics, are the prime enablers of the distributed power framework. Among switched power systems, dc/ac inverters are the most widely adopted solution to interface DERs with the ac power network. DC/AC inverters provide a flexible platform to inject active and reactive power into the grid in the grid-following (GFL) mode or provide voltage and frequency support at the point of common coupling (PCC) in the grid-forming mode (GFM). The primary focus of this work is on the GFL mode of operation. However, many of the proposed concepts can be readily adapted to GFM operation with little or no change.

The main function of the GFL inverter is to track a pre-determined power set point. This power set point generally reflects specific economic objectives related to power efficiency, such as tracking the maximum power point in photovoltaics or providing ancillary services to the power grid [2], [3], [4]. However, maintaining an adequate stability margin and satisfactory performance is often challenging due to the undesired dynamical artifacts caused by nonlinearities, switching distortion, and uncertainties in the system. Furthermore, grid disruptions, which are common in weak grids and microgrids, only exacerbate these difficulties. Therefore, operating a GFL inverter connected to a weak grid involves the following key research focuses.

- 1) *Damping the Filter Resonance*: A major problem with the GFL inverter is the considerable resonance that arises in inverter and line dynamics. This is mainly due to the underdamped modes of the inverter filter, particularly the *LCL* filter.
- 2) *Mitigating Harmonics*: Nonlinear loads, interactions with the weak grid, and switched devices can all contribute to harmonics of fundamental frequency. It is essential to suppress these harmonics in the current waveform to ensure that the quality of the output current waveform is maintained.
- 3) *Reliable Synchronization Scheme*: Effective operation of the GFL inverter requires a synchronization scheme that can lock on to the grid voltage and maintain stability and phase lock, when faced with grid disturbances, such as

sudden changes in voltage/frequency, abrupt phase shifts, and voltage imbalances.

- 4) *Power Tracking and Stability*: Under weak grid conditions, it is challenging to ensure effective power tracking and stability. Variability in system parameters, such as line impedance, which often occurs in weak grid scenarios, requires a robust approach to stability.
- 5) *Grid Fault Ride-Through*: Demonstrating the ability of the inverter to withstand and operate through grid faults is critical to overall reliability and resilience.

These areas are central to improving the reliability and efficiency of GFLs in weak grid environments. In what follows, we will offer a concise overview of the aforementioned topics.

Resonance, whether caused by the underdamped *LCL* filter or the interaction between the inverter's *LC* filter and the inductive transmission line, can lead to instability. Active damping techniques provide a promising solution to mitigate filter resonance and improve stability, without relying on loss-inducing components [5], [6], [7], [8], [9], [10], [11]. Using virtual impedance to dampen the resonance of the *LCL* filter is a method that is intuitive, efficient, and easy to implement. This technique utilizes feedback measurements from the filter states, such as capacitor voltage or inductor current, to imitate the effects of a loss-inducing circuit element, such as a resistor, on the inverter's output voltage and current. The virtual impedance technique has been proved to be effective in enhancing the damping characteristics of the filter and the stability margins of the GFL inverter [5], [6], [7], [8]. More recently, passivity-based approaches to active damping have gained popularity [9], [10], [11], [12]. Passivity-based active damping is rooted in the concept of a dissipative system within control theory. This approach typically guarantees stability and robustness under a variety of operating conditions and parameter changes, which are common in weak grid scenarios. Passivity-based damping methods, although more complex than virtual impedance, offer a more comprehensive analytical framework and advanced damping schemes [11], [12]. Although active damping methods are effective in reducing filter resonance, they can interfere with the functioning of the current closed loop and phase-locked loop (PLL). If not adjusted correctly, these methods can have a detrimental effect on closed-loop bandwidth, synchronization quality, low-frequency disturbance rejection, and the ability to track reference power in steady state [6].

Grid codes [13], [14] require GFL inverters to suppress harmonics of the fundamental frequency and inject a distortion-free current into the grid. This is generally achieved using multifrequency proportional–resonance (PR) controllers [15], [16], [17]. Theoretically, high-gain PR compensators provide better harmonic attenuation and a faster transient response, while increasing the PR damping reduces the attenuation factor but improves the PR sensitivity to changes in harmonic frequency [15], [16], [17]. The systematic PR control design is usually based on the harmonic attenuation factor and the phase margin (PM) specification at the corresponding harmonic frequency [16], [17]. Although this approach provides the basis for tuning the PR gain and damping, it does not capture the interaction between the PR compensator, weak grid, and the inverter filter. This can cause resonance and instability for high values of PR gain and

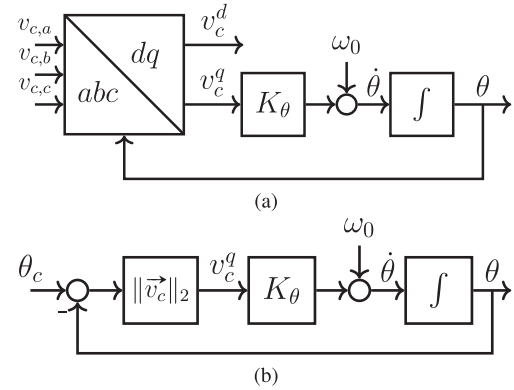


Fig. 1. (a) Conventional three-phase PLL system that include *abc* to *dq* transform, PLL loop filter  $K_\theta$ , and voltage controlled oscillator (integrator). (b) Linearized model of the PLL in (a) that is frequently used for stability and performance analysis of the PLL.

damping factor. Therefore, PR designs include a second step in which the closed-loop transient is tuned through trial and error on both the experimental and simulation platforms [18], [19].

Most GFL control designs employ a variation of the synchronous reference frame phase-locked loop (SRF-PLL), as shown in Fig. 1(a), to synchronize with the grid voltage [20]. The traditional SRF-PLL, depicted in Fig. 1(a), originates from the field of communication systems [21]. In this design, it is implicitly assumed that the phase angle of the input signal, denoted  $\theta_c$  in Fig. 1(b), is independent of the phase angle  $\theta$  generated by the SRF-PLL. In typical GFL applications, this assumption is only valid when the inverter is connected to a stiff grid with negligible line impedance [22], [23], [24], [25], [26]. Under this condition, the voltage phase angle remains dynamically separate from the SRF-PLL angle. However, in the presence of a weak grid and substantial line impedance, the input phase angle  $\theta_c$  in Fig. 1(b) becomes strongly coupled to the PLL dynamics and phase angle  $\theta$  [27]. Consequently, synchronization algorithms based on traditional SRF-PLL are sensitive to voltage fluctuations in the grid and unreliable when there are low-order filter resonance, harmonics, unbalanced, and weak grid conditions [28]. Kulkarni and John [29] suggested a technique for tuning the PLL parameters to balance the PLL synchronization bandwidth and the robustness to voltage unbalance and grid harmonics. Furthermore, the authors in [30] and [31] used an adaptive notch filter to reduce the oscillations of the PLL phase angle in a polluted ac system. Shakerighadi et al. [22] employed a nonlinear time-varying framework for assessing the stability of the SRF-PLL and proposed an adaptive solution to improve stability bounds under frequency and phase disturbances. Islam et al. [23] proposed an adaptive Clarke transform algorithm to accurately track the phase angle of the grid under unbalanced voltage and phase condition. In addition, there is a large body of literature investigating different variations of the Kalman filter to improve the quality of synchronization [24], [25], [26].

Recently, the development of an inertial PLL (IPLL) has emerged as a promising method to enhance the transient response and stability margin of SRF-PLL [32], [33]. The IPLL incorporates a virtual swing equation into the standard SRF-PLL structure. This integration enhances the SRF-PLL's ability to

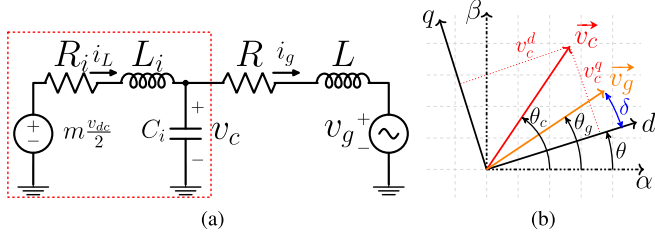


Fig. 2. (a) Inverter averaged model with an output  $RLC$  filter, interfaced to the grid via  $RL$  impedance. (b)  $dq$  rotating frame.

handle frequency deviations more effectively during transient conditions. Finally, there is increasing research on power synchronization techniques for GFL operation [34]. These techniques, commonly used in grid-forming inverters, are being explored as alternatives to traditional SRF-PLL in GFL operations.

Research on GFL control has been extensive, yet the existing literature typically deals with the aforementioned challenges separately, even though they are closely coupled or related and stem from the same underlying dynamical system. Furthermore, some popular design techniques, such as virtual impedance, SRF-PLL, and virtual inertia, involve reusing familiar concepts and components from different fields. Although this approach is intuitive, it can impose artificial restrictions on the inverter's dynamics and limit the peak performance.

The primary contribution of this article is an innovative and comprehensive framework for GFL closed-loop modeling, stability and performance analyses, control design, and control implementation. This framework stands out from the existing literature because of its unified approach to tackling the GFL control issues. Essentially, we evaluate robust stability, zero steady-state tracking, harmonic attenuation, synchronization, frequency transients, inertial response, active damping of filter resonance, and the influence of coupled inverter dynamics on stability and performance using the core components of the closed-loop structure. The unified approach in the proposed framework allows us to determine the fundamental tradeoffs and bottlenecks between the different control objectives and subsequently design the controllers to achieve the proper tradeoff. The following outlines the structure of this article and provides an overview of each section's primary focus and contribution.

The rest of this article is organized as follows. Section II outlines the key dynamic equations and the context for evaluating the GFL control objectives. In Section III, we propose the closed-loop structure in Fig. 2(a) where the transmission line dynamics forms the *plant*, and the inverter dynamics is treated as an actuator. The primary challenge in the proposed model arises from the coupled multi-input multi-output (MIMO) closed-loop dynamics. We utilize the algebraic structure of the closed loop to characterize the underlying coupled MIMO system in terms of a nominal two separate single-input single-output (2-SISO) closed loop with multiplicative MIMO perturbation. As we show, this formulation allows us to clearly isolate the effect of coupled dynamics on the GFL closed loop. Section IV expresses the performance objectives, stability, and robust stability conditions for the proposed MIMO closed loop using direct specifications on the

nominal 2-SISO closed loops derived in Section III. This section examines the influence of dynamical coupling on the stability and performance of the GFL inverter and provides a solution to reduce the effect of coupling on the closed loop. Furthermore, this section introduces an innovative synchronization method that relies only on the disturbance rejection characteristics of the feedback controller and effectively omits the need for an additional PLL system. The proposed synchronization scheme offers a systematic approach to achieve inertia, robustness to grid disturbances, and high-frequency harmonic attenuation. Furthermore, we show that our synchronization technique remains effective even under asymmetrical grid fault. Section V explores and quantifies the fundamental tradeoff between stability margins and control objectives, such as reference tracking, grid disturbance rejection, and damping high-frequency resonance, all based on closed-loop sensitivity analysis. This section demonstrates that linear control design inevitably faces certain performance limitations. As a result, a well-founded control design relies on balancing these desired objectives. In Section VI, we present a control design example that meets the stability and performance criteria established in this article. In addition, we show how the closed-loop dynamics of the inverter can be integrated into the feedback controller to implement the proposed feedback controllers. Finally, Section VII concludes this article.

In the simulation and experimental sections, we focus on key aspects of our proposed framework. The first experiment explores control designs that achieve different tradeoffs between harmonic attenuation and PR-induced filter resonance. This test confirms the fundamental limitations on GFL performance, as discussed and quantified in Section V. The second experiment evaluates the resilience and transient response of the proposed synchronization scheme in the presence of frequency anomalies common in weak grids. In the third experiment, we showcase the system's robustness against asymmetrical faults, demonstrating how the control design effectively counters the resulting harmonics and matches the asymmetrical fault ride-through capabilities of the decoupled double synchronous reference frame (DDSRF) PLL. The fourth experiment examines the robust stability of our controller, based on the novel criteria from Section IV-B. Here, we compare its stability margins with popular active damping techniques that use capacitor voltage and grid current feedback (GCFB) and show improvement in the robust stability margin. Finally, we evaluated the low voltage ride-through capability (LVRT), showing that the system operates reliably even when the grid voltage drops to 30% of its nominal value.

The proof of the main results, presented in the form of propositions, can also be found in the Appendix.

## II. GFL PROBLEM SETTING

We study the GFL control in the context of two connected voltage sources, as shown in Fig. 2(a). Here,  $v_c$  is the inverter's output capacitor voltage, and  $v_g$  denotes the grid voltage. The  $RL$  impedance between  $v_c$  and  $v_g$  represents the combined effect of the transmission line impedance, the grid impedance (for the weak grid), and the grid side inductor of the  $LCL$  filter (if the  $LCL$  filter is used). The controlled voltage source  $m \frac{v_{dc}}{2}$  is the

cycle-averaged model of the inverter switching node, where the modulation signal  $m \in [-1, 1]$  controls the output voltage of the switching node [35], [36]. The inverter's output  $LC$  filter is represented by  $C_i$ ,  $L_i$ , and the equivalent series resistor  $R_i$ . Furthermore,  $i_L$  is the current that flows through  $L_i$  and  $R_i$ . The line and inverter dynamics in Fig. 2(a) are given by

$$L \frac{di_g}{dt} = v_c - v_g - R i_g, \quad (1)$$

$$L_i \frac{di_L}{dt} = \frac{v_{dc}}{2} m - v_c - R_i i_L, \quad C_i \frac{dv_c}{dt} = i_L - i_g. \quad (2)$$

In this work, we adopt the direct-quadrature ( $dq$ ) rotating frame to represent the above dynamics. The  $dq$  frame allows us to:

- 1) use the same notation, analysis, and design for one-phase and three-phase inverter systems;
- 2) transform the sinusoidal tracking problem into a dc tracking problem;
- 3) manipulate the phase directly;
- 4) avoid nonlinear operations, such as phase-shifting/scaling [37], that are common in stationary frame control methods.

In the  $dq$  frame, the line and inverter dynamics in (1) and (2) are transformed into

$$L \frac{d\vec{i}_g^{dq}}{dt} = \vec{v}_c^{dq} - \vec{v}_g^{dq} - R \vec{i}_g^{dq} - L \dot{\theta} \begin{bmatrix} -i_g^q \\ i_g^d \end{bmatrix}^\top \quad (3)$$

$$L_i \frac{d\vec{i}_L^{dq}}{dt} = \frac{v_{dc}}{2} m^{dq} - \vec{v}_c^{dq} - R_i \vec{i}_L^{dq} - L_i \dot{\theta} \begin{bmatrix} -i_L^q \\ i_L^d \end{bmatrix}^\top$$

$$C_i \frac{dv_c^{dq}}{dt} = i_L^{dq} - i_g^{dq} - C \dot{\theta} \begin{bmatrix} -v_c^q \\ v_c^d \end{bmatrix}^\top. \quad (4)$$

In the above,  $\dot{\theta}$  denotes the angular frequency of the  $dq$  rotating frame, and each vector  $f^{dq} = [f^d, f^q]^\top$  comprises the corresponding  $d$  and  $q$  signal components, as shown in Fig. 2(b) [37]. In this article, we primarily use the Laplace transform of the  $dq$  dynamics in (3) and (4) given as

$$\vec{\hat{i}}_g = G_L(s) \left( \vec{\hat{v}}_c - \vec{\hat{v}}_g \right) \quad (5)$$

$$\vec{\hat{v}}_c = G_v(s) \left( \vec{\hat{i}}_L - \vec{\hat{i}}_g - C_i \dot{\theta} \begin{bmatrix} -v_c^q \\ v_c^d \end{bmatrix}^\top \right)$$

$$\vec{\hat{i}}_L = G_i(s) \left( \frac{v_{dc}}{2} \vec{\hat{m}} - \vec{\hat{v}}_c - L_i \dot{\theta} \begin{bmatrix} -i_L^q \\ i_L^d \end{bmatrix}^\top \right) \quad (6)$$

where

$$G_L(s) = \frac{\begin{bmatrix} s + \lambda & \omega_0 \\ -\omega_0 & s + \lambda \end{bmatrix}}{L(s^2 + 2\lambda s + \lambda^2 + \omega_0^2)}, \quad \lambda = \frac{R}{L} \quad (7)$$

$$G_v(s) = \frac{1}{C_i s}, \quad \text{and} \quad G_i(s) = \frac{1}{L_i s + R_i}. \quad (8)$$

We use the hat symbol to denote Laplace domain signals and omit the  $dq$  superscript for vector signals. We assume that all vector signals are expressed in the  $dq$  frame, unless otherwise specified.

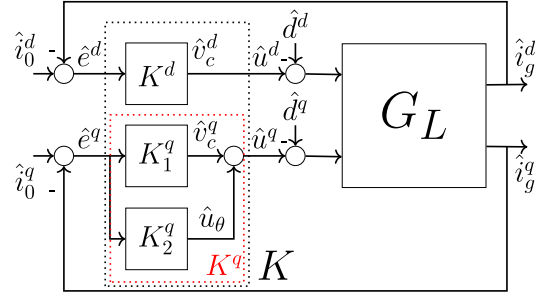


Fig. 3. Control structure with diagonal feedback controller  $[K^d, K^q]$ , MIMO line dynamics  $G_L$ , and exogenous inputs  $[\hat{i}_0^d, \hat{i}_0^q]^\top$  and  $[\hat{d}^d, \hat{d}^q]^\top$ .

Finally, the steady-state operating set-points for the GFL are typically specified in terms of power. However, to exploit the fast, rich, and linear dynamics of voltage and currents in (5) and (6), we map the power reference  $(P_0, Q_0)$  into the corresponding current set-points  $\{i_0^d, i_0^q\}$  as

$$\begin{bmatrix} i_0^d \\ i_0^q \end{bmatrix} = \frac{\Phi_{\{1,3\}}}{\|\vec{v}_c(t)\|^2} \begin{bmatrix} v_c^d & v_c^q \\ v_c^q & -v_c^d \end{bmatrix} \begin{bmatrix} P_0 \\ Q_0 \end{bmatrix} \quad (9)$$

where  $\Phi_1 = 1$  for single-phase and  $\Phi_3 = 2/3$  for three-phase system. The conventional PLL dynamics, such as that shown in Fig. 1(b), is responsible for forcing  $v_c^q$  in (9) to zero by generating the proper rotating angle  $\theta$  that aligns the rotating frame's  $d$ -axis with the inverter voltage phasor  $\vec{v}_c$ . This effectively decouples the mapping between the power reference  $\{P_0, Q_0\}$  and corresponding current set-point  $\{i_0^d, i_0^q\}$ .

### III. NEW PERSPECTIVE ON GFL CLOSED LOOP—MIMO CLOSED LOOP AS A PERTURBED 2-SISO SYSTEM

In this work, we evaluate the stability, performance, transient response, and control design of the GFL inverter in terms of the closed-loop system that is formed around the line dynamics  $G_L$ , as shown in Fig. 3. Here,  $G_L$  is the MIMO transfer function in (7), and  $K^d$  and  $K^q = K_1^q + K_2^q$  form the diagonal feedback compensator  $K = \text{diag}(K^d, K^q)$ . Moreover,  $\vec{e} = i_0 - \vec{i}_g$  denotes the tracking error, and  $\vec{u}$  and  $\vec{d}$  are the control effort and the input disturbance to the plant  $G_L$ , respectively. In the following proposition, we define the control effort  $\vec{u} = [u^d, u^q]^\top$  and the input disturbance  $\vec{d} = [d^d, d^q]^\top$  as they appear in Fig. 3 in terms of the capacitor voltage  $\vec{v}_c$ ,  $dq$  rotating frequency  $\dot{\theta}$ , grid voltage  $v_g$ , and grid frequency  $\dot{\theta}_g$ .

*Proposition 3.1:* For the closed-loop structure in Fig. 3, the control effort  $\vec{u}$  and input disturbance  $\vec{d}$  are

$$\begin{bmatrix} u^d \\ u^q \end{bmatrix} = \begin{bmatrix} v_c^d \\ v_c^q \end{bmatrix} + \begin{bmatrix} 0 \\ u_\theta \end{bmatrix}, \quad \begin{bmatrix} d^d \\ d^q \end{bmatrix} = \|\vec{v}_g\| \begin{bmatrix} 1 \\ \int \Delta\omega_g dt \end{bmatrix} \quad (10)$$

where

$$u_\theta(t) = v_0 \int \Delta\omega dt, \quad \Delta\omega = \dot{\theta} - \omega_0, \quad \Delta\omega_g = \dot{\theta}_g - \omega_0 \quad (11)$$

and  $\{v_0, \omega_0\}$  denote the nominal grid voltage (e.g., 120 V rms) and nominal grid frequency (e.g., 60 Hz), respectively.

*Remark 1:* In our proposed framework, we steer away from the conventional approach of using a separate PLL system, such as the one shown in Fig. 1(a), to directly control the  $dq$  rotating angle  $\theta$ . Instead,  $\theta$  is incorporated into the  $K^q$  output signal  $u^q = v_c^q + u_\theta$ , as outlined in (10) and (11), and shown in Fig. 3. Our work takes advantage of three key benefits of this approach. First, our method enables us to formulate the GFL synchronization and frequency transient response as disturbance rejection objectives for the feedback controller (see Section IV-C). This perspective successfully eliminates the need for a separate PLL system. Second, by treating synchronization as a performance objective for the feedback controller, we are able to design the GFL closed loop to achieve a desired balance between the stability margin and the quality of synchronization (see Section V). Finally, our approach guarantees that a robustly stabilizing controller that meets the synchronization criteria will operate reliably in weak grid environments. It is important to note that when using a separate PLL, a robust controller alone does not ensure robust stability or even stability. The reason is that the interaction between the PLL and the grid can reduce the stability margin, leading to instability.

*Remark 2:* The influence of the grid voltage  $\vec{v}_g$  and frequency  $\dot{\theta}_g$  on the GFL closed loop is treated as an input disturbance, denoted by  $\vec{d}$  in (10), to the plant, as shown in Fig. 3. Considering the decentralized approach to GFL operation in this study, we assume that the magnitude of the grid voltage  $\|\vec{v}_g\|$  and the grid frequency  $\dot{\theta}_g$ , in (10) and (11), is not known or measured. This assumption precludes the use of feedforward methods for mitigating grid disturbances. However, by implementing a disturbance rejection control framework, we can significantly mitigate the effects of disturbance  $\vec{d}$ . As a result, it is practical to base our control design in this article on a nominal disturbance model. We proceed with the assumption that  $\|\vec{v}_g\|$  and  $\dot{\theta}_g$  are generally constant, but may experience deviations, harmonics, and other disturbances common in weak grid scenarios. Therefore, in line with (10), we model the input disturbance as

$$\begin{bmatrix} \hat{d}^d \\ \hat{d}^q \end{bmatrix} \approx v_0 \begin{bmatrix} 1/s \\ \Delta\omega_g/s^2 \end{bmatrix} + \vec{\eta}(s) \quad (12)$$

where  $\hat{d}^d$  is a constant and  $\hat{d}^q$  is a ramp disturbance. In addition,  $\eta(s)$  represent the unmodeled disturbances. By adopting the nominal disturbance model in (12), we prioritize the attenuation of disturbances within a specific frequency domain profile, essentially tailoring the performance characteristics of the controller to the expected disturbance.

In the context of Fig. 3, the closed-loop transfer functions between the exogenous inputs  $\{\vec{i}_0, \vec{d}\}$  and the grid-current  $\vec{i}_g$ , tracking error  $\vec{e}$ , and control effort  $\vec{u}$  are

$$\vec{i}_g = \vec{i}_0 - S(\vec{i}_0 + G_L \vec{d}), \quad \vec{e} = S(\vec{i}_0 + G_L \vec{d}) \quad (13)$$

$$\vec{u} = KS(\vec{i}_0 + G_L \vec{d}) \quad (14)$$

where

$$S = (I_2 + G_L K)^{-1} \quad (15)$$

is the closed-loop MIMO *sensitivity* transfer function, and  $I_2$  denotes the  $2 \times 2$  identity matrix.

For a given feedback controller  $K$ , (13)–(15) uniquely determine the closed-loop stability, steady-state performance, and transient response to grid disturbance  $\vec{d}$ . However, the MIMO characteristics of  $G_L$  and  $S$  make the control design and analysis of closed-loop systems in (13) and (14) significantly more intricate than a SISO system. Therefore, optimization-based methods, such as  $\mathcal{H}_\infty$ , are well suited to address MIMO control synthesis. However, in this article, we use innovative algebraic manipulations to isolate the effect of coupled MIMO dynamics on closed-loop stability and performance. We achieve this by transforming the MIMO system into a nominal 2-SISO system with a multiplicative perturbation that embodies the effect of coupled MIMO dynamics. As we show throughout this article, the proposed method enables us to address the performance and stability of MIMO closed loop in terms of a nominal 2-SISO system.

The feedback controller  $K$  in Fig. 3 is diagonal by design choice, and the MIMO nature of closed loop is due to  $G_L$  in (7). We decompose  $G_L$  into a SISO part  $\tilde{G}_L$ , and multiplicative coupled perturbation  $(I_2 + E)$  as

$$G_L = \tilde{G}_L(I_2 + E) \quad (16)$$

where

$$\tilde{G}_L = \frac{(s + \lambda)/L}{s^2 + 2\lambda s + \lambda^2 + \omega_0^2}, \quad E = (G_L - \tilde{G}_L I_2) \tilde{G}_L^{-1}. \quad (17)$$

Using the SISO factorization of plant in (16), we break down the closed-loop sensitivity in (15) into a 2-SISO component and a coupled MIMO perturbation.

*Proposition 3.2:* (a) *SISO Factorization of Sensitivity:* We factor the MIMO sensitivity transfer function  $S$  in (15) into a 2-SISO sensitivity transfer function  $\tilde{S}$  and coupled MIMO dynamics  $\mathcal{X}_c$  and  $\Gamma$  as

$$S = \tilde{S} \mathcal{X}_c \Gamma \quad (18)$$

where the 2-SISO sensitivity transfer function  $\tilde{S}$  is

$$\tilde{S} = \begin{bmatrix} \tilde{S}^d & 0 \\ 0 & \tilde{S}^q \end{bmatrix} = \begin{bmatrix} (1 + \tilde{G}_L K^d)^{-1} & 0 \\ 0 & (1 + \tilde{G}_L K^q)^{-1} \end{bmatrix} \quad (19)$$

and MIMO dynamics  $\mathcal{X}_c$  and  $\Gamma$  are

$$\mathcal{X}_c = (I_2 + (\Gamma - I_2) \tilde{S})^{-1} \quad (20)$$

$$\Gamma = \tilde{G}_L G_L^{-1} = I_2 + \frac{\begin{bmatrix} -\omega_0^2 & -\omega_0(s + \lambda) \\ \omega_0(s + \lambda) & -\omega_0^2 \end{bmatrix}}{s^2 + 2\lambda s + \lambda^2 + \omega_0^2}. \quad (21)$$

(b) *SISO Characterization of Closed-loop Dynamics:* The effect of the 2-SISO sensitivity  $\tilde{S}$  and coupled MIMO dynamics  $\{\mathcal{X}_c, \Gamma\}$  on the GFL closed-loop dynamics in (13) and (14) is

explicitly given as

$$\vec{i}_g = \vec{i}_0 - \mathcal{X}_c \tilde{S} \left( \Gamma \vec{i}_0 + \tilde{G}_L \vec{d} \right), \quad \vec{e} = \mathcal{X}_c \tilde{S} \left( \Gamma \vec{i}_0 + \tilde{G}_L \vec{d} \right) \quad (22)$$

$$\vec{u} = K \mathcal{X}_c \tilde{S} \left( \Gamma \vec{i}_0 + \tilde{G}_L \vec{d} \right). \quad (23)$$

(c) *Bounding the Closed-loop Coupling*: We can use the SISO sensitivity  $\tilde{S}$  in (19) to bound and reduce the effect of the MIMO coupled dynamic  $\mathcal{X}_c$  on the closed-loop dynamics of the GFL in (22) and (23). In more precise terms, we have

$$\forall \tilde{S}(j\omega) \text{ s.t. } \epsilon(\omega) := \|\tilde{S}(j\omega)\|_2 \|\Gamma(j\omega) - I_2\|_2 < 1 \quad (24)$$

$$\Rightarrow \|\mathcal{X}_c(j\omega) - I_2\|_2 \leq \frac{\epsilon(\omega)}{1 - \epsilon(\omega)}. \quad (25)$$

*Remark 3*: Proposition 3.2 touches on three crucial objectives. First, it deconstructs the MIMO sensitivity  $S$  into a SISO and coupled dynamics. Second, it details the influence of each component on closed-loop dynamics in (22) and (23). Most importantly, it shows the method to mitigate the coupling effect by leveraging  $\tilde{S}$ . Essentially, the bound established in (25) leads to the subsequent decoupling condition

$$\|\epsilon\|_\infty \ll 1 \Rightarrow \|\mathcal{X}_c - I_2\|_\infty \ll 1. \quad (26)$$

Based on above,  $\|\epsilon\|_\infty \ll 1$  results in  $\mathcal{X}_c \approx I_2$ , approximately decoupling (22) and (23) into

$$\vec{e} = \tilde{S}(\Gamma \vec{i}_0 + \tilde{G}_L \vec{d}), \quad \vec{u} = K \tilde{S}(\Gamma \vec{i}_0 + \tilde{G}_L \vec{d}). \quad (27)$$

*Remark 4*: Referring to the definition of  $\epsilon$  in (24), the decoupling condition in (26) is equivalent to the following upper bound on the magnitude of the 2-SISO sensitivity:

$$\|\tilde{S}(j\omega)\|_2 < \frac{1}{\|\Gamma(j\omega) - I_2\|_2} = \frac{\|(\omega + j\lambda)^2 - \omega_0^2\|_2}{\omega_0 \sqrt{(\omega + \omega_0)^2 + \lambda^2}} \quad \forall \omega. \quad (28)$$

The above bound is uniquely shaped by  $\lambda$  and, as shown in Fig. 4(a), the bound becomes less stringent (allowing larger magnitudes of  $\tilde{S}$ ) when  $\lambda$  is higher, which corresponds to predominantly resistive line impedances. This relaxation also occurs as  $\omega$  increases beyond the fundamental frequency  $\omega_0$ , regardless of the line characteristics  $\lambda$ . Essentially, to meet the decoupling condition, it is sufficient to maintain a small sensitivity within the lower frequency range, typically  $[0, 2\omega_0]$ . Note that reducing the sensitivity  $\tilde{S}(j\omega)$  at any frequency is equivalent to raising the controller gain at the same frequency, as evident in (19).

In the rest of this work, we use the SISO sensitivity transfer function  $\tilde{S}$  in (19) and the decoupled closed-loop dynamics in (27) as a basis for stability and performance analysis.

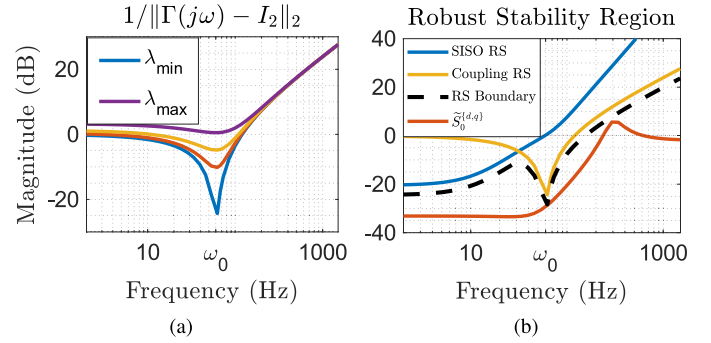


Fig. 4. (a) Upper bound in (28) for different values of  $\lambda$ . The lower values of  $\lambda$  correspond to smaller upper bounds. (b) RS boundary, as shown by the dashed line, consists of two distinct upper bounds: the SISO upper bound (35) and the coupling upper bound. Any nominal closed-loop sensitivity  $\tilde{S}_0$  that remains below the RS boundary is considered to have RS property.

#### IV. CHARACTERIZATION OF STABILITY, PERFORMANCE, AND FUNDAMENTAL LIMITATIONS ON CONTROL DESIGN IN TERMS OF NOMINAL SISO SENSITIVITY

##### A. Conditions on SISO Sensitivity for Nominal Stability of GFL MIMO Closed Loop

In this section, we transform the nominal stability condition for the GFL's MIMO closed loop into a set of simpler-to-check conditions based on the nominal SISO sensitivity  $\tilde{S}$  in (19).

*Proposition 4.1*: The internal stability of the MIMO closed loop in Fig. 3 is guaranteed if the following conditions hold.

(a) *Stability of  $\tilde{S}$* : The two independent SISO sensitivities  $\{\tilde{S}^d, \tilde{S}^q\}$  in (19) have stable poles.

(b) *Magnitude Condition*:  $\epsilon$  in (24) satisfies the decoupling condition  $\|\epsilon\|_\infty < 1$ , or equivalently,  $\tilde{S}$  satisfies (28).

In the next section, we derive the robust stability conditions for the MIMO closed loop based on the SISO sensitivity.

##### B. Conditions on SISO Sensitivity for Robust Stability of the GFL MIMO Closed Loop

Proposition 4.1 outlines the stability conditions for the GFL closed loop based on the nominal value of the line impedance. However, it is often challenging to accurately measure or estimate the line impedance. Furthermore, in the case of a weak grid, the line impedance is prone to change with the grid condition. Our control framework provides robust stability (RS) even in the face of uncertain line impedance. It functions effectively under weak grid conditions and remains stable without the need for precise knowledge of the line impedance.

Typically, the exact value of the line impedance is not known, but we can specify the uncertainty intervals  $\Pi_L$  and  $\Pi_R$  for the line inductance and the line resistance as

$$L \in \Pi_L = [L_{\min}, L_{\max}], \quad R \in \Pi_R = [R_{\min}, R_{\max}], \quad (29)$$

where the minimum and maximum anticipated line inductance and resistance are denoted by  $\{L_{\min}, L_{\max}\}$ , and  $\{R_{\min}, R_{\max}\}$ , respectively. In this context, a robustly stabilizing feedback controller must satisfy Proposition 4.1 for all possible SISO plants  $\tilde{G}_L$  that are generated by sets  $\Pi_L$  and  $\Pi_R$  in (29). We

achieve this by forming the set that encompasses all possible SISO plants, which we label as  $\Pi_G$ . Subsequently, we define the nominal plant, denoted as  $\tilde{G}_{L0}$ , for the impedance uncertainty intervals outlined in (29). Finally, we detail the RS conditions for the set  $\Pi_G$  based on the nominal SISO sensitivity formed by the nominal plant  $\tilde{G}_{L0}$ .

The set of all possible SISO line dynamics, denoted as  $\Pi_G$ , is determined by the uncertainty sets  $\Pi_R$  and  $\Pi_L$  in (29) as

$$\Pi_G = \left\{ \tilde{G}_L(s) = \frac{(s + \lambda)/L}{s^2 + 2\lambda s + \lambda^2 + \omega_2} \mid L \in \Pi_L, \lambda \in \Pi_\lambda \right\} \quad (30)$$

where

$$\Pi_\lambda = \left[ \lambda_{\min} = \frac{R_{\min}}{L_{\max}}, \lambda_{\max} = \frac{R_{\max}}{L_{\min}} \right]. \quad (31)$$

Moreover, we define the nominal SISO plant, represented by  $\tilde{G}_{L0}$ , for the given uncertainty sets  $\Pi_L$  and  $\Pi_\lambda$  as

$$\tilde{G}_{L0} = \frac{(s + \lambda_0)/L_0}{s^2 + 2\lambda_0 s + \lambda_0^2 + \omega_0^2} \quad (32)$$

where

$$L_0 = 2 \frac{L_{\min} L_{\max}}{L_{\min} + L_{\max}}, \quad \lambda_0 = \frac{\lambda_{\max} L_{\max} + \lambda_{\min} L_{\min}}{L_{\min} + L_{\max}}. \quad (33)$$

Subsequently, the nominal SISO sensitivity for  $\tilde{G}_{L0}$  is

$$\tilde{S}_0 = \begin{bmatrix} \tilde{S}_0^d & 0 \\ 0 & \tilde{S}_0^q \end{bmatrix} = \begin{bmatrix} (1 + \tilde{G}_{L0} K^d)^{-1} & 0 \\ 0 & (1 + \tilde{G}_{L0} K^q)^{-1} \end{bmatrix}. \quad (34)$$

The feedback controller  $K = \text{diag}(K^d, K^q)$  in (34) is robustly stabilizing if the closed-loop system maintains stability despite any perturbation of the nominal plant  $\tilde{G}_{L0}$  in (32) within the set of all possible perturbed line dynamics  $\Pi_G$ . In the following proposition, we present the robust stability conditions for the GFL MIMO closed loop in terms of the nominal SISO sensitivity  $\tilde{S}_0$  in (34).

**Proposition 4.2:** The closed loop in Fig. 3 is robustly stable with respect to the set of all possible line dynamics  $\Pi_G$  in (30) if the nominal sensitivity  $\tilde{S}_0$  in (34) satisfies the following:

- the stability conditions in part (a) of Proposition 4.1;
- the following two bounds:

$$\|\tilde{S}_0(j\omega)\|_2 < \frac{1 - \|W_1(j\omega)\|_2 \|W_3(j\omega)\|_2}{\|W_2(j\omega)\|_2} \quad \forall \omega \quad (35)$$

$$\|\tilde{S}_0(j\omega)\|_2 < \frac{\|(\omega + j\lambda_{\min})^2 - \omega_0^2\|_2}{\omega_0 \sqrt{(\omega + \omega_0)^2 + \lambda_{\min}^2}} \quad \forall \omega. \quad (36)$$

where

$$W_1 = \frac{(1/L_0 - 1/L_{\max})s + (\lambda_0/L_0 - \lambda_{\min}/L_{\max})}{(s + \lambda_0)/L_0} \quad (37)$$

$$W_2 = \frac{2(\lambda_{\max} - \lambda_0)s + (\lambda_{\max}^2 - \lambda_0^2)}{s^2 + 2\lambda_0 s + \lambda_0^2 + \omega_0^2}, \quad \text{and} \quad W_3 = \frac{\omega_{\text{bw}}}{s + \omega_{\text{bw}}}. \quad (38)$$

In this proposition,  $\{L_0, \lambda_0\}$  are the nominal parameters of (33),  $\{L_{\max}, \lambda_{\max}, \lambda_{\min}\}$  are the same as in (29) and (31), and  $\omega_{\text{bw}}$  represents the closed-loop bandwidth for the nominal SISO system.

**Remark 5:** The upper bound outlined in (35) is based on the RS condition for the nominal SISO closed loop. On the other hand, (36) arises from the RS condition for the perturbations of the coupling dynamics, as detailed in the proof. As illustrated in Fig. 4(b), the RS bound for the SISO closed loop tends to be more restrictive at lower frequencies. Meanwhile, the RS constraint for coupling dynamics becomes more significant around and above the fundamental frequency  $\omega_0$ . Furthermore, when line inductance increases (which corresponds to a smaller  $\lambda$  value), the constraint in (28) becomes more restrictive at higher frequencies. This trend is clearly depicted in Fig. 4(a). As a result of these observations, the RS conditions outlined in this section indicate that, particularly in inductive lines, the closed-loop system should maintain a minimum bandwidth of  $2\omega_0$  (120 Hz) to ensure robust stability.

### C. Conditions on SISO Sensitivity for Reference Tracking and Synchronization

The primary objective of the GFL inverter is to *synchronize* and *inject* the required power into the grid while maintaining *power quality* (i.e., suppress harmonic and high-frequency disturbances). These objectives are given concisely in terms of closed loop in Fig. 3 as

$$\lim_{t \rightarrow \infty} \vec{e}(t) = 0, \quad \lim_{t \rightarrow \infty} v_c^q(t) = 0, \quad \frac{\|\vec{e}(j\omega)\|_2}{\|\vec{w}(j\omega)\|_2} \ll 1 \quad \forall \omega \quad (39)$$

where  $\vec{w} = \Gamma \vec{i}_0 + \tilde{G}_L \vec{d}$ . In the above,  $\vec{e} = 0$  represents the desired zero steady-state tracking error, and  $v_c^q = 0$  signifies the steady-state synchronization that decouples the mapping between power and current in (9). Furthermore, the inequality in (39) represents a key objective aimed at reducing the effect of closed-loop input signals, represented by  $\vec{w}$ , on the tracking error  $\vec{e}$  throughout the frequency spectrum. This is crucial to ensure that the current waveform remains clear and free of high-frequency distortions.

The GFL objectives in (39) can be formulated in terms of closed-loop SISO sensitivity transfer function  $\tilde{S}$  as

$$\lim_{s \rightarrow 0} \tilde{S} \vec{w} s = 0, \quad \lim_{s \rightarrow 0} [0 \ K_1^q] \tilde{S} \vec{w} s = 0, \quad \|\tilde{S}(j\omega)\|_2 \ll 1 \quad \forall \omega. \quad (40)$$

The above equation is based on applying the final value theorem to  $\vec{e}$  in (27), and  $\vec{v}_c^q = [0 \ K_1^q] \vec{e}$  (see Fig. 3). The inequality in (40) simply follows from (27). The following proposition uses the definition of  $\tilde{S}$  in (19) and the grid disturbance model in (12) to convert the objectives in (40) into the conditions of the feedback controller  $K$ .

**Proposition 4.3:** a) We achieve  $\lim_{t \rightarrow \infty} \vec{e} = 0$ , if and only if  $\tilde{S}^d$  has at least one zero and  $\tilde{S}^q$  has at least two zeros at the

origin. This is equivalent to  $K^d$  having at least one pole and  $K^q$  having at least two poles at the origin.

b) We achieve  $\lim_{t \rightarrow \infty} v_c^q = 0$  (synchronization) if and only if  $K_1^q/K_2^q$  in Fig. 3 possesses at least two zeros at the origin.

c) We can reduce the effect of grid side disturbance  $\vec{d}$  on the tracking error  $\vec{e}$  at any specific frequency, using a high-gain feedback controller. This approach is effective within the closed-loop bandwidth, and the feedback controller  $K$  imposes the following upper bound on the attenuation factor:

$$\frac{\|\vec{e}(j\omega)\|_2}{\|\vec{d}(j\omega)\|_2} \leq \frac{1}{\|K(j\omega)\|_2} \quad \forall \omega. \quad (41)$$

*Remark 6:* The above proposition formulates the synchronization objective as a disturbance rejection characteristic of the feedback controller. It also outlines the necessary and sufficient conditions that the controller must satisfy to achieve synchronization. This eliminates the need for separate PLL and allows for a unified closed-loop analysis between the synchronization quality, stability, and performance objectives.

*Remark 7:* Propositions 4.1–4.3 suggest that a high-gain controller can ensure robust stability and produce a clean and distortion-free current waveform by reducing the sensitivity  $\tilde{S}$  across the frequency spectrum. However, in practice, implementing a controller that maintains substantial gain across a broad frequency band is costly and introduces high-frequency noise into the system. Moreover, as discussed in Section V-B, a fundamental constraint called the Bode sensitivity integral (also known as the waterbed effect) limits the use of high-gain controller over a wide frequency range.

#### D. Conditions on Feedback Controller to Shape the Transient Response of Inverter Frequency

DC/AC inverters do not possess inherent inertia; however, numerous studies, especially for grid-forming inverters, have mimicked the inertial response of synchronous generators. Our work provides a general framework that subsumes the inertial response of the inverter as part of the transient response of the closed loop in Fig. 3 to the grid frequency disturbance  $d^q$ .

*Proposition 4.4:* The transient and steady-state responses of the inverter's frequency deviation  $\Delta\omega$  to the grid frequency deviation  $\Delta\omega_g$  are uniquely specified by

$$\Delta\omega = \tilde{T}_\theta^q \Delta\omega_g, \quad \tilde{T}_\theta^q = K_2^q \tilde{G}_L \tilde{S}^q = \frac{K_2^q \tilde{G}_L}{1 + \tilde{G}_L (K_1^q + K_2^q)}. \quad (42)$$

Moreover,  $\tilde{T}_\theta^q$  always assumes the shape of a low-pass filter with unity dc gain.

*Remark 8:* The step responses of  $\tilde{T}_\theta^q$ , such as the rise time, the settling time, the overshoot, and the oscillation, are generalizations of concepts, such as the rate of change of frequency (RoCoF), the frequency nadir (or zenith), and the inertia. Therefore, we can shape the open loop  $K_2 \tilde{G}_L$  in (42) to obtain the desired transient response to grid frequency disturbance  $\Delta\omega_g$ . Specifically, we include the following:

- 1) *Cross-over frequency:* The cross-over frequency of  $K_2^q \tilde{G}_L$  affects both RoCoF and inertia. A lower cross-over frequency improves the inertial response, reduces RoCoF, and attenuates disturbances and harmonics on the inverter frequency.
- 2) *Phase margin:* The PM of  $K_2^q \tilde{G}_L$  influences the overshoot, where a higher PM dampens the transient response and reduces the frequency nadir or zenith.
- 3) *Roll-off rate:* The roll-off rate of  $K_2^q \tilde{G}_L$  above the cross-over frequency specifies the attenuation factor of the grid side disturbances and harmonics on the inverter frequency.

#### V. FUNDAMENTAL LIMITATIONS ON CONTROL DESIGN AND TRADEOFF BETWEEN DISTINCT OBJECTIVES

We use the sensitivity  $\tilde{S}$  to illustrate two primary bottlenecks in the GFL closed-loop control. These limitations and tradeoffs are fundamental and cannot be solved regardless of the control design. However, by understanding them, we can design controllers that can achieve the desired tradeoff.

##### A. Disturbance Attenuation Bottleneck

We cannot attenuate the impact of grid disturbance  $\vec{d}$  on current tracking error  $\vec{e}$ , inverter voltage  $\vec{v}_c$ , and inverter frequency  $\theta$  simultaneously. In fact, reducing the effect of disturbance on one variable inevitably amplifies the disturbance on the other two. We validate this by rewriting the transfer functions between  $\vec{d}$  and  $\{\vec{e}, \vec{u}\}$  in (27) as

$$\begin{bmatrix} \vec{e}^d \\ \vec{e}^q \end{bmatrix} = \tilde{G}_L \begin{bmatrix} \tilde{S}^d & 0 \\ 0 & \tilde{S}^q \end{bmatrix} \begin{bmatrix} \vec{d}^d \\ \vec{d}^q \end{bmatrix}, \quad \begin{bmatrix} \vec{u}^d \\ \vec{u}^q \end{bmatrix} = \begin{bmatrix} \tilde{T}^d & 0 \\ 0 & \tilde{T}^q \end{bmatrix} \begin{bmatrix} \vec{d}^d \\ \vec{d}^q \end{bmatrix}. \quad (43)$$

The transfer functions  $\{\tilde{T}^d, \tilde{T}^q\}$  above are defined as

$$\tilde{T}^d = K^d \tilde{G}_L \tilde{S}^d, \quad \tilde{T}^q = K^q \tilde{G}_L \tilde{S}^q = (K_1^q + K_2^q) \tilde{G}_L \tilde{S}^q \quad (44)$$

and together with the sensitivities  $\{\tilde{S}^d, \tilde{S}^q\}$ , they satisfy the following algebraic constraints:

$$\tilde{T}^d + \tilde{S}^d = 1, \quad \tilde{T}^q + \tilde{S}^q = 1. \quad (45)$$

We want to minimize the magnitude of  $\{\tilde{S}^q, \tilde{S}^q\}$  through a broad frequency range to reduce the impact of the disturbance  $\vec{d}$  on the tracking error  $\vec{e}$  in (43) and attain perfect current reference tracking (27). Furthermore, the decoupling and stability of the closed-loop MIMO dynamics in Propositions 3.2 and 4.1 are based on reducing the magnitude of  $\{\tilde{S}^q, \tilde{S}^q\}$ . However, based on the algebraic constraint in (45), reducing  $\{\tilde{S}^q, \tilde{S}^q\}$  increases  $\{\tilde{T}^d, \tilde{T}^q\}$  toward 1 creating a unity gain path between  $\vec{d}$  and  $\vec{u}$  in (43). Considering that  $u^d = v_c^d$  and  $u^q = v_c^q + u_\theta$ , this demonstrates a fundamental tradeoff in which attenuating the distortion and harmonics caused by grid disturbances  $\vec{d}$  on the tracking error  $\vec{e}$  amplifies the effect of grid disturbances on  $u_\theta$  and  $\vec{v}_c$ .



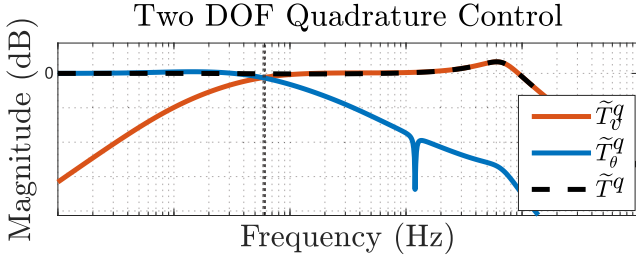


Fig. 5. Quadrature closed-loop  $\tilde{T}^q$  is comprised of low pass  $\tilde{T}_\theta^q$  and bandpass  $\tilde{T}_v^q$ . This attenuates disturbances on  $u_\theta$  beyond  $\tilde{T}_\theta^q$  cutoff frequency (dotted line) by shifting the high-frequency disturbances to  $v_c^q$ .

In GFL operation, we are primarily concerned with the quality of the current waveform, so it is plausible to minimize  $\{\tilde{S}^d, \tilde{S}^q\}$  over a wide frequency range and compromise the quality of the inverter voltage in favor of a harmonic and distortion-free current waveform. However, in the  $q$ -loop, this can lead to distortion of  $u_\theta$  by high-frequency grid disturbances and potentially destabilize inverter operation. Our proposed closed-loop structure can solve this problem.

1) *Inverter Frequency Disturbance Immunity*: The  $dq$  signals are calculated based on the angle of the rotating frame. Therefore, any disturbance and harmonics in  $\theta$  will distort the  $dq$  signals and potentially destabilize the inverter. In this section, we leverage the parallel structure of the  $q$ -axis controller, as shown in Fig. 3, to enhance the resilience of  $u_\theta$  and consequently  $\theta$  against grid disturbances.

As discussed in Proposition 4.4,  $\tilde{T}_\theta^q$  forms a unity-gain low-pass filter between  $\Delta\omega_g$  and  $\Delta\omega$ . Therefore, it attenuates the impact of grid distortions and harmonics above the cutoff frequency. Subsequently, reducing the bandwidth of  $\tilde{T}_\theta^q$  improves the robustness of  $\theta$  against high-frequency grid disturbances. Simultaneously, based on (40) and (43), we want to minimize  $\tilde{S}^q$  across a broad frequency range to achieve harmonic and distortion-free  $\hat{e}^q$ . Balancing these two requirements—low bandwidth for  $\tilde{T}_\theta^q$  and minimize  $\tilde{S}^q$  across a wide frequency range—imposes a unique design challenge for the parallel quadrature controller  $K^q = K_1^q + K_2^q$ . We formalize this design constraint on the  $q$ -axis controller by rewriting the algebraic constraint in (45) as

$$1 - \tilde{S}^q = \tilde{T}^q = \tilde{T}_\theta^q + \tilde{T}_v^q \quad (46)$$

where

$$\hat{v}_c^q = \tilde{T}_v^q \hat{d}^q, \quad \tilde{T}_v^q = K_1^q \tilde{G}_L \tilde{S}^q = \frac{K_1^q \tilde{G}_L}{1 + \tilde{G}_L (K_1^q + K_2^q)} \quad (47)$$

is the transfer function between  $d^q$  and  $v_c^q$ . The algebraic constraint in (46) suggests that the sum of  $\tilde{T}_\theta^q$  and  $\tilde{T}_v^q$  should equal one over a broad frequency range. This range is defined by the bandwidth of the closed-loop transfer function  $\tilde{T}^q$ . Therefore,  $\tilde{T}_v^q$  needs to function as a bandpass filter with unity gain between the cutoff frequencies of  $\tilde{T}_\theta^q$  and  $\tilde{T}^q$ , as illustrated in Fig. 5. Taking into account the parallel structure of  $K^q$  and the definition of  $\tilde{T}_\theta^q$  and  $\tilde{T}_v^q$ ,  $K_1^q$  and  $K_2^q$  should satisfy the following constraint

within closed-loop bandwidth:

$$\tilde{T}_\theta^q \approx \frac{K_2^q}{K_1^q + K_2^q} \text{ (low pass)} \quad \tilde{T}_v^q \approx \frac{K_1^q}{K_1^q + K_2^q} \text{ (bandpass)}. \quad (48)$$

Intuitively,  $K_2^q$  should have high gain within the low frequency, whereas  $K_1^q$  should have high gain in the bandpass region.

2) *Operation Under Asymmetrical Fault*: During an asymmetrical fault, the PCC voltage becomes unbalanced. Under these conditions, we can represent the unbalanced three-phase voltage as a superposition of the positive sequence, the negative sequence, and the zero sequence as [38]

$$\begin{aligned} v_g^a &= a \|v_g\| \cos(\dot{\theta}_g t) + b \|v_g\| \cos(\dot{\theta}_g t + \psi) + v_g^0 \\ v_g^b &= a \|v_g\| \cos(\dot{\theta}_g t - \frac{2\pi}{3}) + b \|v_g\| \cos(\dot{\theta}_g t + \psi - \frac{4\pi}{3}) + v_g^0 \\ v_g^c &= a \|v_g\| \cos(\dot{\theta}_g t - \frac{4\pi}{3}) + b \|v_g\| \cos(\dot{\theta}_g t + \psi - \frac{2\pi}{3}) + v_g^0 \end{aligned} \quad (49)$$

where  $a$  and  $b$  are amplitudes of positive- and negative-sequence unbalanced voltages with respect to the  $\|v_g\|$ . Furthermore,  $v_g^0$  represents the zero sequence, and  $\psi$  is the phase angle of the negative sequence with respect to the positive sequence. In a synchronized  $dq$  frame, (49) is [39]

$$\begin{aligned} v_g^d &= \|v_g\| (a \cos(\delta) + b \cos(2\dot{\theta}_g t - \delta + \psi)) \\ v_g^q &= \|v_g\| (a \sin(\delta) - b \sin(2\dot{\theta}_g t - \delta + \psi)) \end{aligned} \quad (50)$$

where  $\delta$  represent the phase angle between the grid positive-sequence voltage phasor and synchronized  $dq$  frame, as shown in Fig. 2(b). Following along the lines of a Proposition 3.1, and based on (50), the input disturbance under asymmetric fault is:

$$\begin{bmatrix} d^d \\ d^q \end{bmatrix} = v_0 \left( a \begin{bmatrix} 1 \\ \int \Delta\omega_g dt \end{bmatrix} + b \begin{bmatrix} \cos(2\dot{\theta}_g t - \delta + \psi) \\ -\sin(2\dot{\theta}_g t - \delta + \psi) \end{bmatrix} \right). \quad (51)$$

Compared with the nominal disturbance model in (10), the asymmetric fault imposes an additional second-harmonic component on the disturbance  $\vec{d}$  in the  $dq$  frame. The second harmonic, unchecked, propagates to the output current (27) and results in the third harmonic in the stationary frame [38]. We can attenuate the effect of the second-harmonic disturbance on  $\vec{e}$  by reducing the sensitivity  $\tilde{S}$  at  $2\dot{\theta}_g$  [see (19) and (43)]. As shown in (41), this is achieved by cascading a high-gain PR controller, as detailed below, with the controller  $K$ :

$$K_{PR} = 1 + k_2 \frac{4\xi_2 \omega_0 s}{s^2 + 4\xi_2 \omega_0 s + 4\omega_0^2}, \quad \xi_2 \geq \max_{\Delta\omega_g} \left\| \frac{\Delta\omega_g}{\omega_0} \right\|. \quad (52)$$

Based on (41), increasing the PR gain  $k_2$  leads to a more effective attenuation of second-harmonic disturbances. Furthermore, the choice of the damping factor  $\xi_2$  is influenced by the anticipated maximum deviation of the grid frequency from its nominal value

$\omega_0$ . When  $\xi_2$  is set to a higher value, the PR controller becomes more efficient in mitigating harmonics caused by asymmetrical faults, especially in scenarios where the frequency of the grid strays from the nominal value, a common situation in weak grids. However, as we show in Section V-B and in experiments, higher values of  $k_2$  and  $\xi_2$  induce a high frequency resonance.

Cascading the PR compensator with the feedback controller  $K$  is not sufficient to guarantee effective performance during an asymmetrical fault. Furthermore, it is necessary to maintain a harmonic-free rotational frame angle  $\theta$ . Based on the analysis in Section V-A1, the algebraic constraint in (46) and the definition of  $\tilde{T}_v^q$  in (47), cascading the PR compensator with  $K_1^q$  bring  $\|\tilde{T}_v^q(2j\omega_0)\|_2$  close to one, while  $\tilde{T}_\theta^q$  exhibits a notch behavior at  $2\omega_0$ , as shown in Fig. 5(a). The notch response of  $\tilde{T}_\theta^q$  at  $2\omega_0$  allows the inverter frequency to filter out the second harmonic created by the asymmetric fault, allowing the fault ride-through.

*Remark 9:* The DDSRF-PLL is an advanced algorithm that is used to accurately track the phase and frequency of the grid voltage under distorted or unbalanced conditions [40], [41]. DDSRF-PLL employs two synchronous frames: one aligns with the positive sequence and the other with the negative sequence. This approach allows the DDSRF-PLL to effectively detect and synchronize with the grid frequency, particularly under unbalanced conditions. Our proposed control design and closed-loop structure can work under unbalanced grid conditions and has the same performance as DDSRF-PLL without the need for an extra synchronous reference frame. The robust stability argument in Section IV-B guarantees the robustness of our approach in the face of grid uncertainties and fluctuations. In the experiments section, we compare DDSRF-PLL with our proposed approach in terms of performance and sensitivity to grid uncertainties.

### B. High-Frequency Resonance

Ideally, we want to keep the magnitude of sensitivity small at all frequencies to maintain perfect power tracking and disturbance rejection (13), minimizing the effect of coupling (25) and robust stability (28). However, the Bode sensitivity integral (88) indicates a fundamental limitation on the total amount of sensitivity reduction throughout the frequency spectrum for any viable control design [42]. Essentially, regardless of the control design, reducing the sensitivity at a lower frequency for asymptotic reference tracking, reducing the coupling effect, and synchronization will increase the sensitivity at other frequencies, causing a peak in the sensitivity transfer function, as shown in Fig. 6. The peak sensitivity  $M_s = \|\tilde{S}\|_\infty$ , is directly proportional to the overshoot and oscillation in the transient response of the GFL inverter and is inversely correlated with the robustness of the closed loop to the uncertainty of the plant. In the following proposition, we quantify how the performance of GFL places a theoretical limit on the minimum value that  $M_s$  can achieve.

*Proposition 5.1:* For any stable  $\tilde{S}$  in (19), the peak sensitivity  $M_s$  for each SISO loop  $\tilde{S}^q$  and  $\tilde{S}^q$  is lower bounded by

$$\frac{1}{\omega_T - \omega_B} \left( \left| \int_0^{\omega_B} \ln |\tilde{S}^{\{d,q\}}| d\omega \right| - \frac{3}{4}\omega_T \right) \leq \ln M_s \quad (53)$$

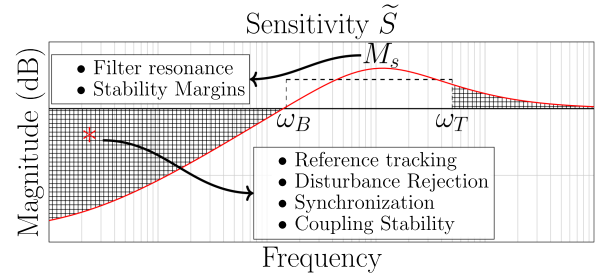


Fig. 6. Shape of  $\tilde{S}$  at different frequencies directly indicates performance objectives and stability margins.

where  $\omega_B$  and  $\omega_T$  are shown in Fig. 6 and defined as

$$\forall \omega \in [0, \omega_B], \ln |\tilde{S}| \leq 0 \quad (54)$$

$$\forall \omega \in [\omega_T, \infty), \|\tilde{G}_L K(j\omega)\|_2 \leq \frac{1}{2} \left( \frac{\omega_T}{\omega} \right)^2. \quad (55)$$

*Remark 10:* Equation (53) connects the transient response and the stability margin in the form of the peak sensitivity  $M_s$  to the low-frequency performance metrics, as shown in Fig. 6. Moreover, it presents all the knobs available to achieve a tradeoff between conflicting control objectives. Note that

$$2 \arcsin \left( \frac{1}{2M_s} \right) [\text{rad}] \leq \text{PM}, \quad \frac{M_s}{M_s - 1} \leq \text{GM} \quad (56)$$

where to limit the oscillation and maintain the gain margin (GM) and PM of at least 6 dB and  $30^\circ$ , it is sufficient to keep  $M_s$  less than 2 [42]. Consequently, it is desirable to shape the sensitivity so that the left-hand side of (53) becomes less than  $\ln 2$ . Based on (53) for any linear GFL control design, only four general and primary methods and their combinations exist to reduce the peak sensitivity. These methods are as follows:

- 1) *Closed-loop bandwidth:* Increasing  $\omega_T$ , reduces the peak sensitivity by increasing both  $0.75\omega_T$  and the denominator in (53). Taking into account the definition of  $\omega_T$  in (55), the open-loop gain cross-over frequency is below  $\omega_T$ , and  $\omega_T$  can be taken as a rough approximation of the closed-loop bandwidth. This approach leads to more noise and harmonics in the voltage of the capacitor and the inverter frequency.
- 2) *Effective control bandwidth:* Decreasing  $\omega_B$  constrains the sensitivity integral limits in (53) to a smaller frequency range while increasing the denominator. Based on (54),  $\omega_B$  represents the frequency range where  $\tilde{S}$  is less than one and the feedback reduces the effect of exogenous inputs [see (13)]; hence, we call  $\omega_B$  an effective control bandwidth. We can reduce  $\omega_B$  by decreasing the open-loop gain just below the gain cross-over frequency.
- 3) *Low-frequency performance:* The sensitivity integral is the main contributor to the peak sensitivity lower bound in (53). We can reduce the integral by increasing the sensitivity within the effective control bandwidth  $\omega_B$ . However, this sacrifices the quality of reference tracking, disturbance rejection, and synchronization. More explicitly, we

can use following approximation of  $\tilde{S}$  within  $[0, \omega_B]$ :

$$\left| \int_0^{\omega_B} \ln |\tilde{S}^{d,q}| d\omega \right| \approx \int_0^{\omega_B} \ln |\tilde{G}_L| + \ln |K^{d,q}| d\omega \quad (57)$$

to capture the effect of the high-gain controller on the sensitivity integral. As is evident, PR harmonic compensators and high-gain pure integrators negatively impact the peak sensitivity by increasing above integral.

- 4) *Uniform sensitivity distribution*: Uniform distribution of  $\tilde{S}$  within the  $[\omega_B, \omega_T]$  frequency range leads to smaller  $M_s$  by making the inequality in (53) tighter. We employed (90) in the proof of the peak sensitivity inequality, and under the uniform distribution of  $\tilde{S}$  within  $[\omega_B, \omega_T]$  this inequality changes to equality. Therefore, we can flatten the sensitivity transfer function by using the lead compensator within the  $[\omega_B, \omega_T]$  frequency range and reduce  $M_s$ .

## VI. FRAMEWORK FOR INVERTER CONTROL IMPLEMENTATION AND SYNTHESIS

The controller  $K$  in Fig. 3 incorporates the dynamics of the inverter from (6), which we have not taken into account in previous sections for a simplified analysis of performance and stability. In this section, we will first provide an example of a control design for  $\{K^d, K_1^q, K_2^q\}$  that meets the stability and performance criteria discussed earlier. We will then demonstrate how the dynamics of the inverter and their associated closed-loop shape the controllers and their implementation.

### A. Design of the Feedback Controllers

We adopt the following control designs for  $K^d$  and  $K_1^q$ :

$$K^d = \left( \frac{L\omega_d \sqrt{\omega_d^2 + \lambda^2}}{\alpha_d s} \right) \left( \frac{s + \alpha_d \omega_d}{s + \omega_d / \alpha_d} \right), \quad \alpha_d \leq 1 \quad (58)$$

$$K_1^q = \left( \frac{L\omega_q^2}{\alpha_q} \frac{s + \alpha_q \omega_q}{s + \omega_q / \alpha_q} \right) \left( \frac{s}{(s + \lambda)(s + \omega_\theta / 5)} \right), \quad \alpha_q \leq 1 \quad (59)$$

$$K_2^q = \left( \frac{L\omega_\theta^2}{\alpha_\theta s^2} \frac{s + \alpha_\theta \omega_\theta}{s + \omega_\theta / \alpha_\theta} \right) \left( \frac{s^2 + 2\lambda s + \lambda^2 + \omega_0^2}{s + \lambda} \right), \quad \alpha_\theta \leq 1 \quad (60)$$

where  $L$  and  $\lambda$  are same as in (7).  $K^d$  in (58) is composed of an integrator and a lead compensator and includes two tunable parameters  $\{\alpha_d, \omega_d\}$ . For  $2\pi 120 \leq \omega_d$ , the  $d$ -axis open-loop transfer function  $K^d \tilde{G}_L$  achieves a cross-over frequency close to  $\omega_d$  and a PM close to

$$90^\circ + \arcsin \frac{1 - \alpha_d^2}{1 + \alpha_d^2} - \arctan \frac{\omega_d}{\lambda}. \quad (61)$$

Subsequently, for the given  $K^d$  in (58), the sensitivity  $\|\tilde{S}^d\|$  as defined in (19) is less than one below  $\omega_d$ , and also satisfies the decoupling condition in Proposition 3.2(c) and the stability condition in Proposition 4.1. Moreover, the integrator in  $K^d$

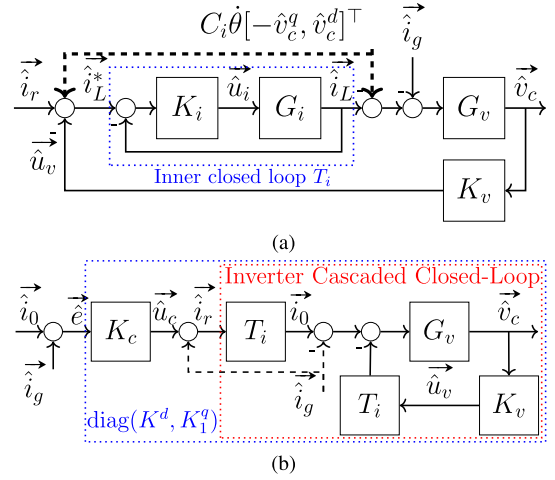


Fig. 7. (a) Cascaded control structure with nested inner current closed loop  $T_i$  and outer voltage loop compensator  $K_v$ . (b) Algebraic equivalent of a nested architecture with series compensator  $K_c$ .

automatically fulfills the zero steady-state tracking condition in Proposition 4.3(a). Note that smaller values of  $\alpha_d$  result in robust stability and lower high frequency filter resonance.

$K_1^q$  in (59) is composed of a lead compensator and a bandpass filter and includes three tunable parameters  $\{\alpha_q, \omega_q, \omega_\theta\}$ .  $\omega_q$  and  $\omega_\theta$  denote the desired cross-over frequency for  $K^q \tilde{G}_L$  and  $K_2^q \tilde{G}_L$ , which specifies the bandpass frequency range  $[\omega_\theta, \omega_q]$  for  $\tilde{T}_v^q$ , as shown in Fig. 5. For  $2\pi 120 \leq \omega_q$ , the  $q$ -axis open-loop transfer function  $K^q \tilde{G}_L$  achieves a cross-over frequency close to  $\omega_q$  and a PM close to

$$\arcsin \frac{1 - \alpha_q^2}{1 + \alpha_q^2}. \quad (62)$$

The controller  $K_2^q$  in (60) includes two integrators and together with  $K_1^q$  in (59), they satisfies the zero steady-state tracking and synchronization objectives of Proposition 4.3. Furthermore, the proposed controller shapes the  $K_2^q \tilde{G}_L$  as

$$K_2^q \tilde{G}_L = \frac{\omega_\theta^2}{\alpha_\theta s^2} \frac{(s + \alpha_\theta \omega_\theta)}{(s + \omega_\theta / \alpha_\theta)}. \quad (63)$$

Based on Proposition 4.4,  $K_2^q \tilde{G}_L$  is the open-loop transfer function for  $\tilde{T}_\theta$ . Therefore, based on Remark 8, the cross-over frequency  $\omega_\theta$  is directly proportional to the closed-loop bandwidth of  $\tilde{T}_\theta$ . Therefore, we achieve a more inertial response with smaller values of  $\omega_\theta$ . In addition, increasing the PM by decreasing  $\alpha_\theta$  reduces the frequency nadir (zenith) by damping the overshoot of the transient response.

To implement the proposed controllers, we have to understand the underlying embedding of the inverter dynamics and its closed loop into the controllers. In what follows, we use cascaded closed loop to derive one such relation.

### B. Implementing Feedback Controller With Inverter Dynamics

We adopt the cascaded architecture with inner current and outer voltage loops, as shown in Fig. 7(a) to form closed loop around inverter dynamics in (6). Here,  $G_v$  and  $G_i$  represent the

inverter capacitor and inductor dynamics in (6), respectively. In addition, to decouple the inductor dynamics in (6) we employ the feedback linearization by defining the modulation signal as

$$\vec{m} = \frac{2}{v_{dc}} \left( \vec{u}_i + \vec{v}_c + L_i \dot{\theta} [-\hat{i}_L^q, \hat{i}_L^d]^\top \right) \quad (64)$$

where  $\vec{u}_i$  denotes the output of current compensator  $K_i$  in Fig. 7(a), and  $v_{dc}$  is the inverter's input dc voltage. Subsequently, we use  $K_i = (L_i s + R_i)/(\tau_i s)$  to shape the inner closed loop  $T_i$  into a unity gain low-pass filter

$$T_i = \frac{G_i K_i}{1 + G_i K_i} = \frac{1}{\tau_i s + 1}, \quad S_i = 1 - T_i = \frac{\tau_i s}{1 + \tau_i s} \quad (65)$$

where  $1/\tau_i$  is the inner closed-loop bandwidth.

We close the outer voltage loop, as shown in Fig. 7(a), by setting the reference  $\vec{i}_L^*$  for the inner closed loop as

$$\vec{i}_L^* = \vec{i}_r - \vec{u}_v + C_i \dot{\theta} [-v_c^q, v_c^d]^\top. \quad (66)$$

Here,  $\vec{u}_v$  is the output of the diagonal controller  $K_v$ ,  $C_i \dot{\theta} [-v_c^q, v_c^d]^\top$  is the feed-forward term used to decouple the capacitor dynamics in (6), and  $\vec{i}_r$  is the input to the nested closed loop. Subsequently, the proposed nested inverter closed loop results in the following relation between the inputs  $\{\vec{i}_r, \vec{i}_g\}$  and  $\vec{v}_c$ :

$$\vec{v}_c = G_v S_v \left( T_i \vec{i}_r - \vec{i}_g - S_i C_i \dot{\theta} [-v_c^q, v_c^d]^\top \right), \quad \text{where} \quad (67)$$

$$S_v = \begin{bmatrix} S_v^d & 0 \\ 0 & S_v^q \end{bmatrix} = \begin{bmatrix} (1 + G_v T_i K_v^d)^{-1} & 0 \\ 0 & (1 + G_v T_i K_v^q)^{-1} \end{bmatrix}. \quad (68)$$

Finally, we set  $\vec{i}_r$  in (67) as  $\vec{i}_r = \vec{u}_c + \vec{i}_g$ , where  $\vec{u}_c$  denotes the output of diagonal compensator  $K_c = \text{diag}(K_c^d, K_c^q)$ . This transforms the nested architecture in Fig. 7(a) into a natural feedback compensator, as shown in Fig. 7(b), and given by

$$\vec{v}_c = G_v S_v (K_c T_i \vec{e} - S_i (\vec{i}_g + C_i \dot{\theta} [-v_c^q, v_c^d]^\top)). \quad (69)$$

For small values of  $\tau_i$ ,  $S_i$  is negligible over a wide range of frequencies, and therefore,  $S_i (\vec{i}_g + C_i \dot{\theta} [-v_c^q, v_c^d]^\top)$  is insignificant and we omit it from (69). This leads to the following feedback compensator:

$$\begin{aligned} \begin{bmatrix} \hat{v}_c^d \\ \hat{v}_c^q \end{bmatrix} &= \begin{bmatrix} K^d & 0 \\ 0 & K_1^q \end{bmatrix} \begin{bmatrix} \hat{e}^d \\ \hat{e}^q \end{bmatrix}, \quad \begin{bmatrix} K^d & 0 \\ 0 & K_1^q \end{bmatrix} \\ &= G_v T_i \begin{bmatrix} S_v^d K_c^d & 0 \\ 0 & S_v^q K_c^q \end{bmatrix}. \end{aligned} \quad (70)$$

The equation above demonstrates the dependence of the controllers  $K^d$  and  $K_1^q$  on the inverter dynamics, which are represented by  $G_v$ ,  $T_i$ , and  $S_v$ .  $G_v$  and  $T_i$  are already determined in (6) and (65), and  $S_v$  in (68) can only be shaped through the voltage compensator  $K_v$ . Consequently, the controllers  $K^d$

and  $K_1^q$  can only be adjusted by  $K_c$  and  $K_v$ . Therefore, two main questions arise: which transfer functions  $K^d$  and  $K_1^q$  can represent, and how to find the corresponding  $K_v$  and  $K_c$ . We answer these two questions considering the controller of the  $d$ -axis  $K^d$ , and the analysis for the  $q$ -axis is the same. We can expand  $K^d$  in terms of  $K_c$  and  $K_v$  as follows:

$$K^d = G_v T_i S_v^d K_c^d = \frac{D^d(s)}{C_i s (\tau_i s + 1) D^d(s) + N^d(s)} K_c^d \quad (71)$$

where  $N^d(s)$  and  $D^d(s)$  are the numerator and denominator polynomials of voltage compensator  $K_v = N^d(s)/D^d(s)$ , respectively. Considering that  $K_v^d$  and  $K_c^d$  can represent any proper transfer functions, the controller  $K^d$  in (71) can only represent transfer functions of relative degree of at least two. We can relax this condition to include transfer functions with a relative degree of one if  $\tau_i$  is small or equivalently if the inner current loop  $T_i$  has a high enough bandwidth. In this case, we can use the following approximation for (71):

$$K^d \approx \frac{D^d(s)}{C_i s D^d(s) + N^d(s)} K_c^d. \quad (72)$$

On the basis of above, we can easily find  $K_c$  and  $K_v$  for any controller  $\{K^d, K_1^q\}$  with relative degree of at least one. For example, the sample controllers  $\{K^d, K_1^q\}$  in (58) and (59) are implemented using the following  $K_c$  and  $K_v$  controllers:

$$\begin{aligned} K_c^d &= \frac{\omega_d \sqrt{\omega_d^2 + \lambda^2}}{\alpha_d \omega_{LC}^2}, & K_v^d &= \frac{C_i \omega_d (1/\alpha_d - \alpha_d) s}{s + \omega_d \alpha_d} \\ K_c^q &= \frac{\omega_q^2}{\alpha_q \omega_{LC}^2} \frac{s + \alpha_q \omega_q}{s + \omega_q/\alpha_q}, & K_v^q &= C_i \left( \lambda + \frac{\omega_\theta}{5} \right) + C_i \frac{\lambda \omega_\theta}{5 s} \end{aligned} \quad (73)$$

where  $\omega_{LC_i} = 1/\sqrt{LC_i}$ . As a final note, the proposed control design in this section subsumes the virtual impedance methods.

*Neglected Time Delay:* Till this point, we have neglected the time delay present in the inverter model. Generally, inverter dynamics is affected by two primary sources of delay: pulsewidth modulation (PWM) delay, denoted as  $T_{\text{PWM}}$ , and delay due to DSP calculations, represented as  $T_{\text{calc}}$  [43]. In this article, we assume that the sampling frequency  $f_s = 1/T_s$  and the switching frequency  $f_{\text{sw}} = 1/T_{\text{sw}}$  are the same. In this case,  $T_{\text{PWM}} = 0.5T_s$  and  $T_{\text{calc}} = T_s$ , and the total delay is  $T_d = T_{\text{PWM}} + T_{\text{calc}} = 1.5T_s = 1.5/f_s$ . Time delay introduces an additional phase lag into the inverter's open loop, which grows linearly with frequency. This lag can be quantified as  $\phi_d = -T_d \omega = -1.5(\omega/f_s)$  [rad]. Note that by maintaining an appropriate PM for the  $d$ - and  $q$ -axis open loops, as outlined in (61) and (62), we can effectively counteract the extra phase lag caused by time delay around the cross-over frequency. This approach improves the robustness of closed-loop stability against time delays.

## VII. SIMULATION AND EXPERIMENTAL RESULTS

In this section, we demonstrate some of the salient features of the proposed framework through simulations and experiments. The simulations are carried out using the MATLAB Simscape

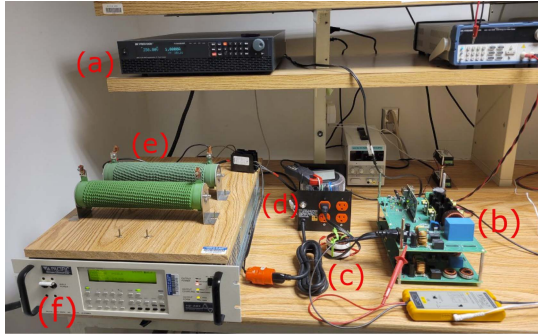


Fig. 8. Experimental setup. (a) DC source (DC link). (b) Inverters. (c) Line inductors. (d) Isolation transformer. (e) Load. (f) AC source (grid simulator).

TABLE I  
SIMULATION AND EXPERIMENTAL PARAMETERS

Parameter	Sym.	Sim.	Expt.	Parameter	Sym.	Value
Filter capacitor	$C_i$	50 $\mu\text{F}$	20 $\mu\text{F}$	Grid voltage (line-rms)	$v_g$	120 V
Filter inductor	$L_i$	1 mH	3 mH	Fundamental Frequency	$\omega_g$	60 Hz
Grid inductor	$L$	1 mH	4.1 mH	Switching frequency	$f_{sw}$	20 kHz
Grid resistance	$R$	1 m $\Omega$	1.4 m $\Omega$	Sampling Frequency	$f_s$	20 kHz

toolbox; as for the experimental results, we used an inverter powered by a TI C2000 series DSP connected to a four-quadrant programmable ac source as a grid (see Fig. 8). Table I lists the parameters used in the simulation and the experiment.

#### A. Design for Harmonic Compensation Vs. Filter Resonance

Reducing  $\|\tilde{S}\|_\infty$  attenuates the effect of grid disturbance  $\vec{d}$  on the output current  $\vec{i}_g$ , see (40) and (43). Our framework suggests a fundamental tradeoff between reducing the sensitivity and increasing the peak resonance  $M_s = \|\tilde{S}\|_\infty$ , see (53). In practice, this shows the inherent limitation of popular PR schemes, where reducing  $\tilde{S}$  and attenuating the disturbance harmonics using the PR controller leads to an increase in peak sensitivity. An increase in  $M_s$  induces filter resonance. This issue is typically addressed by tuning the PR parameters through trial and error. However, our framework provides theoretical ground, based on (53), to improve the tradeoff between harmonic attenuation and filter resonance.

To achieve a better tradeoff between harmonic compensation and filter resonance, i.e., smaller  $M_s$ , we must improve the trade-off bound in (53) by augmenting PR with an additional compensator. Based on (53), reducing effective control bandwidth  $\omega_B$ , less aggressive low-frequency performance, and uniform sensitivity distribution help reduce peak sensitivity. These three objectives are achieved simultaneously by implementing a simple lead compensator of the form  $(s + \alpha\omega_r)/(s + \omega_r/\alpha)$ ,  $\alpha < 1$ , where  $\omega_r$  is close to the resonant frequency.

To validate our approach, we used an ac source with 10% third harmonic distortion. The standalone PR compensation is capable of reducing the third harmonic distortion by 80%, as shown in Fig. 9(b). However, the standalone PR scheme induces

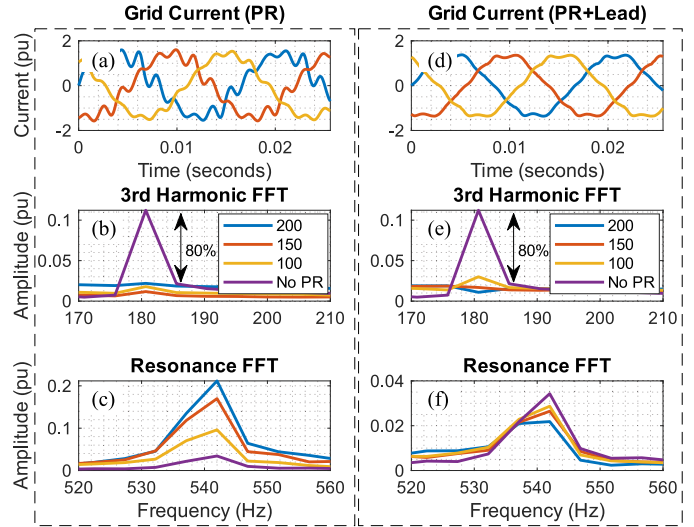


Fig. 9. (a) PR induced current distortion. (b) PR compensators with distinct gains {100, 150, 200} reduce harmonic content by 80%, while (c) triggering filter resonance proportional to PR integral in (57). (d) PR + Lead scheme alleviates current distortion by (e) reducing the harmonic content by 80% and (f) reducing PR-induced filter resonance.

the filter resonance in proportion to the PR gain, as illustrated in Fig. 9(c). The PR+Lead compensation scheme achieves the same third harmonic attenuation as standalone PR, as shown in Fig. 9(e). However, the PR+Lead scheme reduces the filter resonance by at least 60% in Fig. 9(f).

#### B. Designing the Frequency Response to Grid Anomaly

Weak grids are prone to phase and frequency jumps and fluctuations. This can negatively affect the inverter phase angle  $\theta$  and distort the calculation of the  $dq$  signals. In our framework,  $d^q$  represents the grid frequency disturbance, and the algebraic constraint in (46) indicates the fundamental limitation where the effect of  $d^q$  on  $u_\theta$  and  $v_c^q$  cannot be made small simultaneously. Therefore, as stated in Section V-A1, it is desirable that  $\tilde{T}_\theta^q$  take the form of a unity gain low-pass filter that smooths the effect of grid frequency fluctuations on the inverter's frequency while  $\tilde{T}_v^q$  absorbs high frequency noise and harmonics (see Fig. 5(a)).

A series of simulations with different cutoff frequencies for  $\tilde{T}_\theta^q$  [dotted line in Fig. 5(a)] demonstrate that a lower RoCoF and a slower transient response to a unit step change in the grid frequency [see Fig. 10(a)] and grid phase jump [see Fig. 11(a)] are obtained with lower cutoff frequencies. Furthermore, there is a noticeable decrease in the frequency overshoot (zenith) with lower cutoff frequencies. However, unlike the inverter phase and frequency, for lower cutoff frequencies the inverter voltage exhibits a larger excursion for the step change in the grid frequency [see Fig. 10(b) and (c)] and grid phase jump [see Fig. 11(b) and (c)]. This is due to the constraint in (46). Finally, we performed the frequency step change in the experimental setup and observed that the inverter frequency and the  $q$ -axis voltage response in Fig. 12 match the simulation results in Fig. 10. Furthermore, the experimental results in Fig. 12 show that most

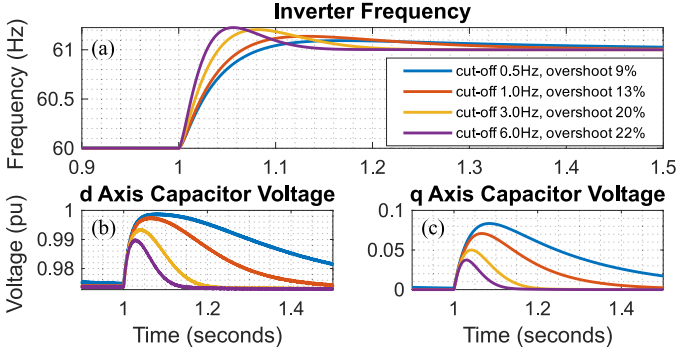


Fig. 10. Transient response to 1 Hz step change in grid frequency.

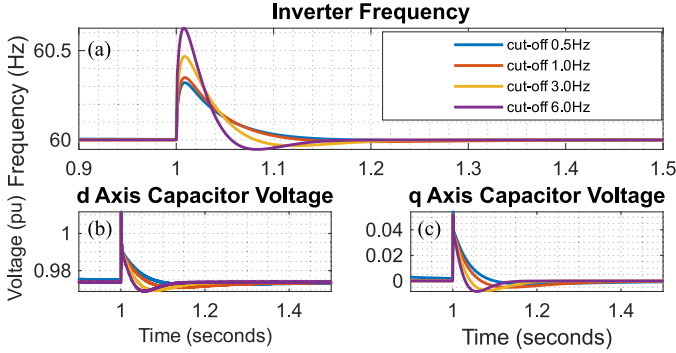


Fig. 11. Transient response to  $5^\circ$  step change in grid phase.

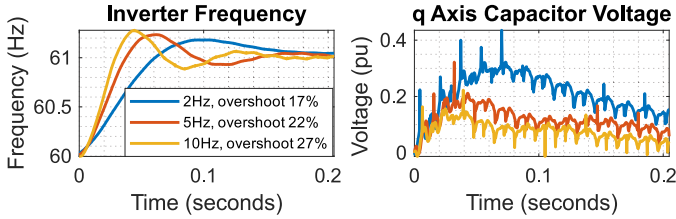


Fig. 12. Transient response of experimental setup to 1 Hz step change in grid simulator frequency.

of the high-frequency distortion is shifted from  $u_\theta$  to  $v_c^q$ . Note that the cutoff frequency of  $\hat{T}_\theta^q$  in the classical sense is inversely correlated with the inertial type of response of the inverter, and we can control the frequency nadir by opting for lower cutoff frequencies.

### C. Design for Asymmetrical Fault

Operating GFL inverters on an unbalanced grid presents significant challenges. The main issue is that the conventional PLL typically struggles to accurately lock onto the grid frequency and follow the positive-sequence phase angle. The DDSRF PLL, as discussed in [40], effectively maintains phase lock with positive sequence even during asymmetric grid faults and can function amidst voltage imbalances distorted by high-order harmonics. However, this level of performance requires the use of two synchronous frames and nonlinear dynamics to properly

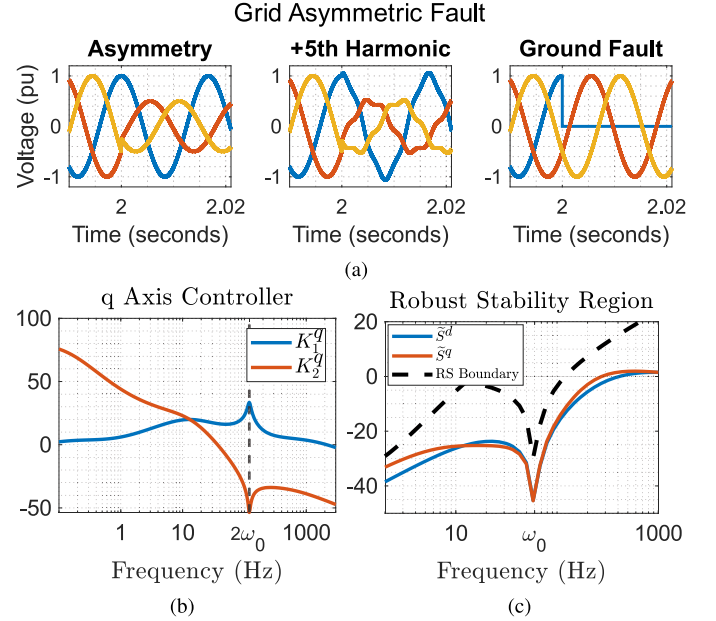


Fig. 13. (a) Three asymmetrical faults investigated in this article: voltage imbalance, voltage imbalance with fifth harmonic distortion, and line-to-ground fault. (b) Parallel  $q$ -axis controller  $K^q = K_1^q + K_2^q$  with 120-Hz PR compensator in  $K_1^q$  and 120-Hz notch filter in  $K_2^q$ . (c)  $d$  and  $q$  closed-loop sensitivities of the E-GFL system, along with the robust stability boundary corresponding to the uncertainty sets in (74).

separate the positive and negative sequences. A key advantage of our proposed control framework is its ability to match the performance of the DDSRF PLL during asymmetrical grid faults, but without the need for an additional synchronous frame or nonlinear dynamics. We accomplish this solely through the use of the PR compensator in the  $q$ -axis controller.

As extensively explained in Section V-A2, asymmetric grid faults manifest as second harmonic disturbances in the  $dq$  frame. By integrating the PR controller, as specified in (52), into  $K^d$  and  $K_1^q$ , we can significantly diminish the impact of this second harmonic on both the output line current  $\vec{i}_g$  and the  $dq$  rotating angle  $\theta$ . Furthermore, the effects of asymmetric distortion on  $dq$  angle  $\theta$  can be further mitigated by cascading a notch filter at  $2\omega_0$  with  $K_2^q$ . In Fig. 13(b), we illustrate the Bode magnitude plot for the components of the  $q$ -axis controller.

In this section, we compare our proposed control method with the DDSRF PLL's performance in three asymmetric fault scenarios. This comparison includes the DDSRF PLL as detailed in [40] incorporated with a second harmonic compensator and an active virtual impedance damping with capacitor voltage feedback (CVFB) similar to that given in [8]. These enhancements are essential because, on its own, the DDSRF PLL lacks the necessary closed-loop stability margins and loop gain for stable functioning and efficient disturbance rejection of second harmonic.

1) *First Scenario*: As shown in Fig. 13(a), two phases operate at 0.5 per unit (p.u.), and the third phase operates at nominal voltage. In this scenario, both our proposed method and the enhanced DDSRF PLL (with virtual impedance and second

harmonic compensator) successfully maintain a clean output line current and a distortion-free  $dq$  rotating frequency, as shown in Fig. 14(a).

2) *Second Scenario*: This involves the same voltage imbalance as the first scenario, but with an additional fifth-order harmonic distortion, as depicted in Fig. 13(b). Again, both our method and the DDSRF PLL manage to maintain a clean rotating frequency and effectively reject the second harmonic in the output current. However, due to the absence of a fifth-order PR compensator, some harmonic distortion remains in the output current, see Fig. 14(b).

3) *Third Scenario (Line-to-Ground Fault)*: In this situation, one of the phases is directly connected to the ground, as shown in Fig. 13(c). In Fig. 14, we observe that our methods again successfully achieve a clean rotating frequency and a distortion-free line current.

These comparisons underscore the effectiveness of our control method in addressing different types of asymmetric fault. The results indicate that the performance of our E-GFL method matches that of the DDSRF PLL, even when the DDSRF is augmented with extra measures, such as virtual impedance active damping for increased stability margin. Notably, our method attains this level of performance without the need for an additional synchronous frame or nonlinear dynamics to separate the positive and negative sequences.

#### D. Robust Stability Under Line Parameter Uncertainty

In Section IV-B, we outlined the conditions required for robust stability when operating with uncertain, yet bounded, line impedance. To confirm these conditions, as proposed in Proposition 4.2, we examine the closed-loop performance and stability for the following sets of uncertainties in line inductance and resistance:

$$L \in \Pi_L = [1 \text{ mH}, 3 \text{ mH}], \quad R \in \Pi_R = [1 \text{ m}\Omega, 200 \text{ m}\Omega]. \quad (74)$$

Considering the uncertainty sets above and referring to (33), the nominal parameters for control design are as follows: inductance  $L_0 = 1.5 \text{ mH}$ ,  $R_0 = 225 \text{ m}\Omega$ , and  $\lambda_0 = 150$ . Using these nominal values along with the robust stability conditions outlined in (35) and (36), we established the Robust Stability (RS) boundary, depicted by the dashed line in Fig. 13(c). To ensure robust stability, the magnitudes of the SISO sensitivities  $\tilde{S}^d$  and  $\tilde{S}^q$  must remain below this RS boundary. We have successfully designed a controller such that the 2-SISO sensitivities, as shown in Fig. 13(c), stay within the confines of the RS boundary. Simulations demonstrate that these controllers maintain stability as the line impedance varies within the uncertainty set. In Fig. 15(a), we present the current reference tracking performance and the inverter frequency response when the step change of 0.2 p.u. is applied to both  $d$  and  $q$  current set-points. This performance is observed at the four extreme points of line impedance variation, namely, the four possible combinations of the highest and lowest values of line inductance and resistance.

To assess the robustness of our proposed E-GFL controller, we compared it with a GFL inverter that uses standard PLL

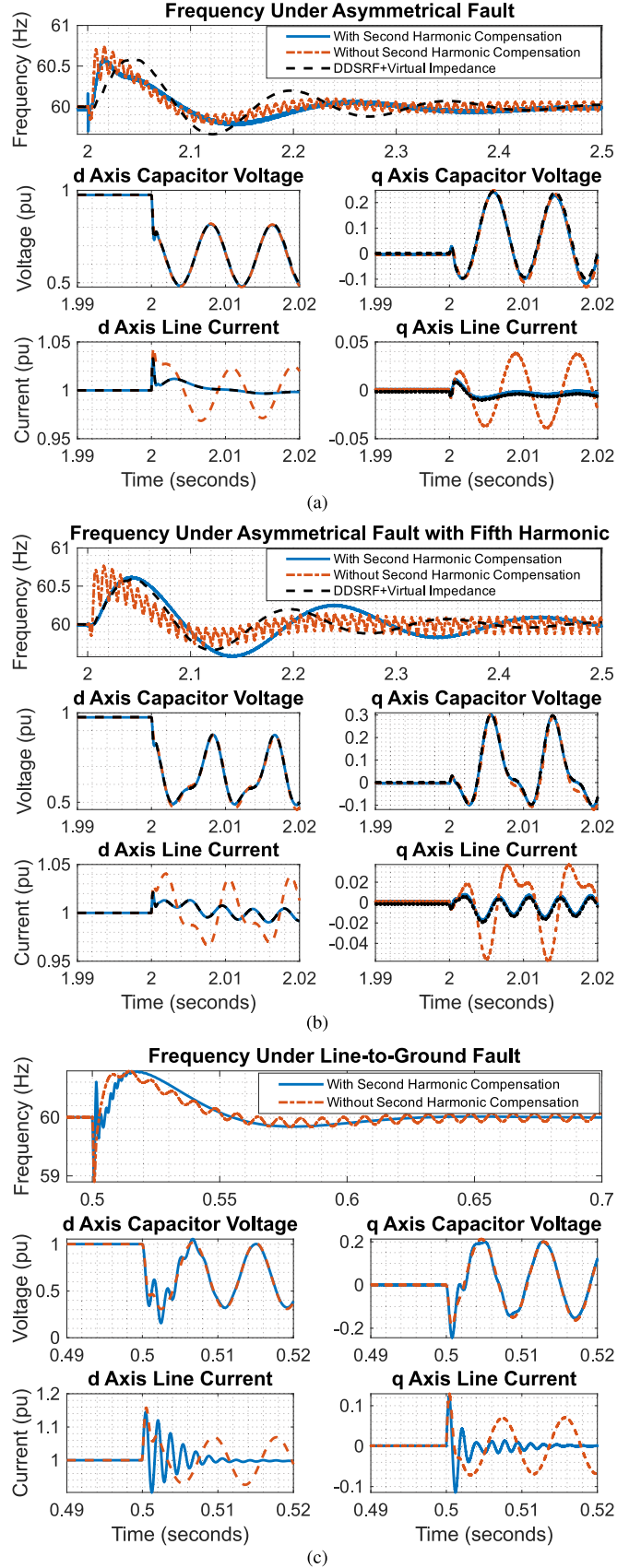


Fig. 14. (a) Asymmetrical fault. (b) Asymmetrical fault with harmonic distortion. (c) Line-to-ground fault. The uncompensated closed-loop response (orange line) is provided for comparison.

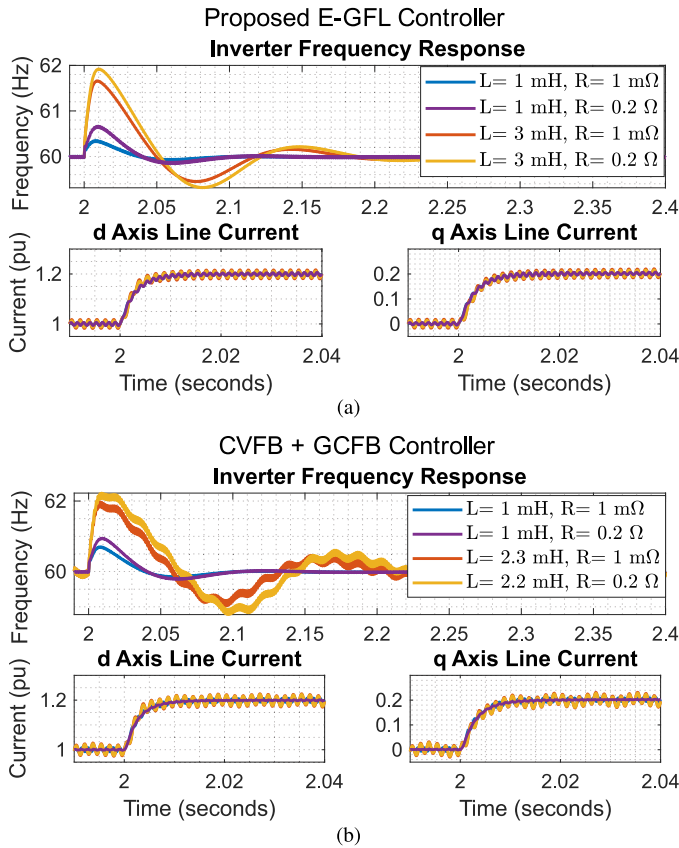


Fig. 15. (a) Proposed E-GFL approach demonstrates its current tracking capabilities and rotating frame frequency response when faced with uncertainties in line impedance. (b) Current tracking performance and frequency response of CVFB+GCFB in face of line impedance uncertainty.

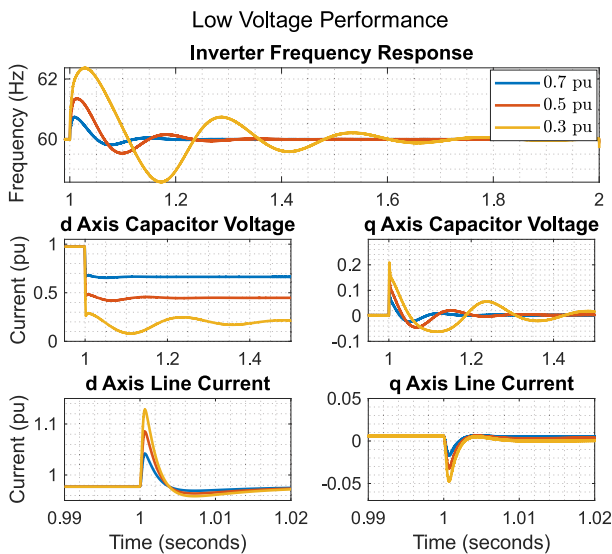


Fig. 16. Our control design successfully provides LVRT capability down to 30% of the nominal voltage value. However, as the voltage dips, the stability margins decrease, which is evident from the increasing oscillations in the system's transient response.

structure, as shown in Fig. 1(a) and a combination of CVFB and GCFB [8] for active damping and stabilization. For fairness in comparison, we used the same nominal line values  $L_0, R_0$ , and  $\lambda_0$  to adjust the control design parameters in both setups. The results are shown in Fig. 15(b), which reveal that the CVFB+GCFB approach performs comparably to the E-GFL at a lower inductance value of  $L = 1$  mH. However, it is observed that the GFL inverter approaches the brink of instability when the inductance reaches approximately 2.3 mH. This finding implies that our proposed method provides a better margin of robustness. Specifically, the closed loop can sustain stability across a range of line inductances approximately 1.5 times greater than that managed by the CVFB+GCFB method. This factor is calculated as  $(3 \text{ mH} - 1 \text{ mH}) / (2.3 \text{ mH} - 1 \text{ mH}) \approx 1.5$ .

### E. Low-Voltage Performance

During peak power demand, the grid may undergo substantial voltage dips. Such voltage sags can inadvertently cause the GFL inverters to disconnect, triggering a chain reaction in which the DERs are progressively cutoff from the grid. This can worsen the situation by further destabilizing the power balance and deepening the voltage drop. Therefore, it is crucial for GFL inverters to have LVRT capability. Our proposed control design successfully achieves LVRT, maintaining operation even when the grid voltage falls to as low as 30% of its nominal value. Fig. 16 illustrates how the proposed controller performs at three different levels of voltage drop. As the voltage dip intensifies, the transient response of the closed-loop system becomes increasingly oscillatory. It is also important to note that the proposed controller starts to lose stability when the voltage drops close to 25% or less of its nominal value.

## VIII. CONCLUSION

We presented a novel and comprehensive framework for GFL control that exploits the algebraic structure of the MIMO line dynamics and captures the effect of coupled dynamics on the stability and performance of the closed loop. The proposed framework embeds the inverter dynamics in the feedback controller and links different performance criteria, such as reference tracking, synchronization, harmonic attenuation, and filter resonance. In future work, we will extend the proposed framework to GFM inverters to accommodate a seamless transition between the GFL and GFM modes of operation.

### APPENDIX

*Proposition 3.1:* The inverter voltage  $\vec{v}_c$  is controllable and is part of  $\vec{u}$ . The grid voltage  $\vec{v}_g$  is not controllable or even measurable. However, in the  $dq$  frame we have

$$\vec{v}_g = \begin{bmatrix} v_g^d \\ v_g^q \end{bmatrix} = \begin{bmatrix} \|v_g\| \cos(\delta) \\ \|v_g\| \sin(\delta) \end{bmatrix} = \begin{bmatrix} \|v_g\| \\ \|v_g\| \delta \end{bmatrix} + \mathcal{O}(\delta^2) \quad (75)$$

where  $\delta = \theta_g - \theta$  is the angle between the grid voltage phasor and the rotating frame, as shown in Fig. 2(b).  $v_g^q$  depends on the orientation of the rotating frame through  $\delta$ , while  $v_g^d$  is close to the magnitude of the grid voltage and is independent



of the rotating frame. We exploit dependence on orientation and the small angle approximation  $\mathcal{O}(\delta^2) \approx 0$  to rewrite  $v_g^q$  as

$$v_g^q = \|v_g\|\delta = \|v_g\| \underbrace{\int (\dot{\theta}_g - \omega_0) dt}_{d^q} - \|v_g\| \underbrace{\int (\dot{\theta} - \omega_0) dt}_{u_\theta} \quad (76)$$

splitting  $v_g^q$  into disturbance  $d^q$  and manipulated variable  $u_\theta$ . However, since we do not have the measurement of  $v_g$ , we approximate it by  $v_0$  in calculating  $u_\theta$ . ■

*Proposition 3.2:* (a) Note that

$$S = (I_2 + \tilde{G}_L K)^{-1} (I_2 + E(I_2 - \tilde{S}))^{-1}. \quad (77)$$

By definition, we replace  $E$  with  $(\Gamma^{-1} - I_2)$  in (77) and factor out  $\Gamma^{-1}$  to get (18). ■

(b) Replace the sensitivity factorization (18) into (13), and (14). (c) We use the Neumann series to get

$$\mathcal{X}_c = (I_2 + (\Gamma - I_2)\tilde{S})^{-1} = I_2 + \sum_{n=1}^{\infty} (-(\Gamma - I_2)\tilde{S})^n.$$

Hence,  $\|\mathcal{X}_c - I_2\|$  satisfies the following bound:

$$\|\mathcal{X}_c - I_2\|_2 \leq \sum_{n=1}^{\infty} \left( \|\Gamma(j\omega) - I_2\| \|\tilde{S}(j\omega)\| \right)^n = \frac{\epsilon(\omega)}{1 - \epsilon(\omega)}.$$

*Proposition 4.1:* Both  $G_L$  and  $K$  are stable transfer functions (we only consider stable controllers); hence, the closed loop in Fig. 3 is internally stable if and only if  $S$  is stable. Stability of  $\tilde{S}$  and  $\mathcal{X}_c$  in (20) guarantees the stability of  $S$  ( $\Gamma$  is always stable). The first condition assumes stability of  $\tilde{S}$ , and the second condition provides the following spectral radius upper bound  $\rho((\Gamma(j\omega) - I_2)\tilde{S}(j\omega)) \leq \epsilon(\omega) < 1 \forall \omega$ , which is the sufficient condition for stability of  $\mathcal{X}_c$ . ■

*Proposition 4.2:* (a) We have  $\tilde{G}_{L0} \in \Pi_G$ . Therefore, if  $\tilde{S}_0$  in (34) is unstable, then there is at least one plant in the set  $\Pi_G$  that leads to instability and violates the RS condition.

(b) We can ensure robust stability if conditions (a) and (b) of Proposition 4.1 are satisfied for all perturbed SISO plants  $\tilde{G}_{Lp} \in \Pi_G$ . To fulfill condition (a), note that the sensitivity for an arbitrary  $\tilde{G}_{Lp} \in \Pi_G$  is

$$\tilde{S}_p = (I_2 + K\tilde{G}_{Lp})^{-1}.$$

We can always represent  $\tilde{S}_p$  for any  $\tilde{G}_{Lp} \in \Pi_G$  in terms of the nominal plant  $\tilde{G}_{L0}$  in (32) as

$$\tilde{S}_p = \left( I_2 + K\tilde{G}_{L0} \frac{1 + \Delta_1 W_1}{1 + \Delta_2 W_2} \right)^{-1} \quad (78)$$

where  $(1 + \Delta_1 W_1)$  represents the uncertainty in zeros of the plant and  $(1 + \Delta_2 W_2)$  expresses the uncertainty in poles of the plant. The transfer functions  $\Delta_1(s)$  and  $\Delta_2(s)$  represent the norm-bounded complex perturbations that satisfy

$$\|\Delta_1(j\omega)\|_\infty \leq 1, \quad \|\Delta_2(j\omega)\|_\infty \leq 1.$$

and the uncertainty weights  $W_1(s)$  and  $W_2(s)$  for the set of perturbed plants  $\Pi_G$  are any transfer functions that satisfy

$$\|W_1(j\omega)\|_2 \geq \max_{\substack{\lambda \in \Pi_\lambda \\ L \in \Pi_L}} \left\{ \left\| \frac{(j\omega + \lambda)/L - (j\omega + \lambda_0)/L_0}{(j\omega + \lambda_0)/L_0} \right\|_2 \right\} \quad \forall \omega$$

$$\|W_2(j\omega)\|_2 \geq \max_{\lambda \in \Pi_\lambda} \left\{ \left\| \frac{(2\lambda j\omega + \lambda^2) - (2\lambda_0 j\omega + \lambda_0^2)}{2\lambda_0 j\omega + \lambda_0^2 + \omega_0^2 - \omega^2} \right\|_2 \right\} \quad \forall \omega. \quad (79)$$

Based on robust control theory [42], the perturbed SISO sensitivity  $\tilde{S}_p$  is stable for all  $\tilde{G}_{Lp} \in \Pi_G$  if

$$\|\tilde{S}_0 W_2\|_2 + \|(I_2 - \tilde{S}_0)W_1\|_2 < 1 \quad \forall \omega \quad (80)$$

where  $\tilde{S}_0$  is the nominal sensitivity in (32), and  $W_1$  and  $W_2$  are any transfer functions that satisfy (79). Although the choices for  $W_1$  and  $W_2$  in (79) are not unique, our proposed weights in (37) and (38) lead to a less conservative robust stability bound in (80). Finally, we use the following approximation to further simplify the RS condition in (80):

$$I_2 - \tilde{S}_0 \approx \frac{\omega_{bw}}{s + \omega_{bw}} = W_3 \rightarrow \|\tilde{S}_0 W_2\|_2 < 1 - \|W_1 W_3\|_2 \quad \forall \omega.$$

Therefore, satisfying (35) guarantees that condition (a) of Proposition 4.1 holds for all perturbed line dynamics.

Now, to ensure that condition (b) of Proposition 4.1 is met for every perturbed plant  $\tilde{G}_{Lp} \in \Pi_G$ , we start by noting two key points. Initially, it is important to recognize that the bound in (28) is exclusively dependent on the parameter  $\lambda$ . Furthermore, for any given  $\lambda \in \Pi_\lambda$  we have

$$\frac{\left\| (\omega + j\lambda_{\min})^2 - \omega_0^2 \right\|_2}{\omega_0 \sqrt{(\omega + \omega_0)^2 + \lambda_{\min}^2}} < \frac{\left\| (\omega + j\lambda)^2 - \omega_0^2 \right\|_2}{\omega_0 \sqrt{(\omega + \omega_0)^2 + \lambda^2}} \quad \forall \omega. \quad (81)$$

Therefore, the most restrictive or the smallest lower bound is associated with the case of  $\lambda_{\min}$ , as shown in Fig. 4(a). Consequently, if the bound specified in (28) is satisfied for  $\lambda_{\min}$ , it will inherently be satisfied for all other potential values of  $\lambda$  within the set  $\Pi_\lambda$ .

*Proposition 4.3:* (a) We achieve zero steady-state error iff the final value condition  $\lim_{s \rightarrow 0} \tilde{S} \vec{w} s = 0$  in (40) is satisfied. We can rewrite the final value condition as

$$\lim_{s \rightarrow 0} \left( \tilde{S} \Gamma \begin{bmatrix} i_0^d & i_0^q \end{bmatrix}^\top + v_0 \tilde{S} \tilde{G}_L \begin{bmatrix} 1 & \Delta \omega_g / s \end{bmatrix}^\top \right) = 0 \quad (82)$$

where we used the disturbance type from (12) and assumed constant reference  $\vec{i}_0$ . It is fairly easy to validate that (82) holds only under the given proposition. ■

(b) We achieve synchronization or  $v_c^q = 0$  iff the final value condition  $\lim_{s \rightarrow 0} [0 \ K_1^q] \tilde{S} \vec{w} s = 0$  in (40) is satisfied. We can rewrite the final value condition as

$$\lim_{s \rightarrow 0} \left[ 0 \ K_1^q \tilde{S}^q \right] \left( \Gamma \begin{bmatrix} i_0^d & i_0^q \end{bmatrix}^\top + v_0 \tilde{G}_L \begin{bmatrix} 1 & \Delta \omega_g / s \end{bmatrix}^\top \right) = 0. \quad (83)$$

Summoning the definition of  $\tilde{S}^q$ , (83) is satisfied if and only if  $K_1^q / K_2^q$  has at least two zeros at the origin. ■

(c) Based on (27), we have

$$\|\vec{\hat{e}}(j\omega)\|_2 \leq \|\vec{\tilde{S}}\Gamma\|_2 \|\vec{\hat{i}}_0(j\omega)\|_2 + \|\vec{\tilde{S}}\vec{\tilde{G}}_L\|_2 \|\vec{\hat{d}}(j\omega)\|_2 \quad \forall \omega. \quad (84)$$

Therefore, the attenuation effect of the proposed closed loop on the input set-point and grid disturbance is

$$\frac{\|\vec{\hat{e}}(j\omega)\|_2}{\|\vec{\hat{i}}_0(j\omega)\|_2} \leq \|\vec{\tilde{S}}(j\omega)\Gamma(j\omega)\|_2, \quad \frac{\|\vec{\hat{e}}(j\omega)\|_2}{\|\vec{\hat{d}}(j\omega)\|_2} \leq \|\vec{\tilde{S}}(j\omega)\vec{\tilde{G}}_L(j\omega)\|_2. \quad (85)$$

Within the control bandwidth, we have  $\vec{\tilde{S}}\Gamma \approx 1/KG_L$  and  $\vec{\tilde{S}}\vec{\tilde{G}}_L \approx 1/K$ , therefore

$$\frac{\|\vec{\hat{e}}(j\omega)\|_2}{\|\vec{\hat{i}}_0(j\omega)\|_2} \leq \frac{1}{\|K(j\omega)G_L(j\omega)\|_2}, \quad \frac{\|\vec{\hat{e}}(j\omega)\|_2}{\|\vec{\hat{d}}(j\omega)\|_2} \leq \frac{1}{\|K(j\omega)\|_2}. \quad (86)$$

The above equation completes the proof. ■

*Proposition 4.4:*  $\hat{u}_\theta = [0 \ K_2^q] \vec{e}$ , and therefore, using (27)

$$\hat{u}_\theta = \begin{bmatrix} 0 & K_2^q \end{bmatrix} \vec{\tilde{S}} \left( \vec{\Gamma} \vec{\hat{i}}_0 + \vec{\tilde{G}}_L \vec{\hat{d}} \right), \quad \text{and} \quad \vec{T}_\theta^q = K_2^q \vec{\tilde{G}}_L \vec{\tilde{S}}^q. \quad (87)$$

Finally, based on Proposition (4.3),  $K_2^q$  mostly includes at least two integrators while  $K_1^q/K_2^q$  has at least two zeros. Therefore,  $\lim_{\omega \rightarrow 0} \vec{T}_\theta^q(j\omega) = 1$ . Moreover,  $K_2^q$  is proper and  $\vec{\tilde{G}}_L$  is strictly proper, hence  $\vec{T}_\theta^q$  rolls off at high frequency, making it a low-pass filter with unity dc gain. ■

*Proposition 5.1:* The nominal sensitivity  $\vec{\tilde{S}}$  is stable with no right half-plane (RHP) zeros; moreover,  $\vec{\tilde{G}}_L K$  is of the relative degree of at least two. Hence, as a direct application of Bode's sensitivity integral, we have

$$\int_0^\infty \ln |\vec{\tilde{S}}(j\omega)| d\omega = 0. \quad (88)$$

We split (88) into three distinct integrals over the frequency range, as shown in Fig. 6, and rewrite it as

$$\left| \int_0^{\omega_B} \ln |\vec{\tilde{S}}| d\omega \right| = \int_{\omega_B}^{\omega_T} \ln |\vec{\tilde{S}}| d\omega + \int_{\omega_T}^\infty \ln |\vec{\tilde{S}}| d\omega. \quad (89)$$

Both of the integrals on the right-hand side are positive, finite, and bounded

$$\int_{\omega_B}^{\omega_T} \ln |\vec{\tilde{S}}| d\omega \leq (\omega_T - \omega_B) \ln M_s, \quad \int_{\omega_T}^\infty \ln |\vec{\tilde{S}}| d\omega \leq \frac{3}{4} \omega_T \quad (90)$$

where the first bound follows from the definition of  $M_s$  and the second is based on the condition in (55). A detailed proof of the second inequality is given in [44]. We derive (53) by replacing (90) with (89). ■

## REFERENCES

- [1] D. Perez-DeLaMora, J. E. Quiroz-Ibarra, G. Fernandez-Anaya, and E. Hernandez-Martinez, "Roadmap on community-based microgrids deployment: An extensive review," *Energy Rep.*, vol. 7, pp. 2883–2898, 2021.
- [2] S. F. Zarei, H. Mokhtari, M. A. Ghasemi, S. Peyghami, P. Davari, and F. Blaabjerg, "Control of grid-following inverters under unbalanced grid conditions," *IEEE Trans. Energy Convers.*, vol. 35, no. 1, pp. 184–192, Mar. 2020.
- [3] F. Blaabjerg, Y. Yang, D. Yang, and X. Wang, "Distributed power-generation systems and protection," *Proc. IEEE*, vol. 105, no. 7, pp. 1311–1331, Jul. 2017.
- [4] Z. Yuan, A. Zecchino, R. Cherkaoui, and M. Paolone, "Real-time control of battery energy storage systems to provide ancillary services considering voltage-dependent capability of DC-AC converters," *IEEE Trans. Smart Grid*, vol. 12, no. 5, pp. 4164–4175, Sep. 2021.
- [5] X. Wang, F. Blaabjerg, and P. C. Loh, "Grid-current-feedback active damping for LCL resonance in grid-connected voltage-source converters," *IEEE Trans. Power Electron.*, vol. 31, no. 1, pp. 213–223, Jan. 2016.
- [6] C. Bao, X. Ruan, X. Wang, W. Li, D. Pan, and K. Weng, "Step-by-step controller design for LCL-type grid-connected inverter with capacitor-current-feedback active-damping," *IEEE Trans. Power Electron.*, vol. 29, no. 3, pp. 1239–1253, Mar. 2014.
- [7] Y. He, X. Wang, X. Ruan, D. Pan, and K. Qin, "Hybrid active damping combining capacitor current feedback and point of common coupling voltage feedforward for LCL-type grid-connected inverter," *IEEE Trans. Power Electron.*, vol. 36, no. 2, pp. 2373–2383, Feb. 2021.
- [8] W. Chen, Y. Zhang, Y. Tu, Y. Guan, K. Shen, and J. Liu, "Unified active damping strategy based on generalized virtual impedance in LCL-type grid-connected inverter," *IEEE Trans. Ind. Electron.*, vol. 70, no. 8, pp. 8129–8139, Aug. 2023.
- [9] X. Wang, Y. He, D. Pan, H. Zhang, Y. Ma, and X. Ruan, "Passivity enhancement for LCL-filtered inverter with grid current control and capacitor current active damping," *IEEE Trans. Power Electron.*, vol. 37, no. 4, pp. 3801–3812, Apr. 2022.
- [10] M. Awal, L. Della Flora, and I. Husain, "Observer based generalized active damping for voltage source converters with LCL filters," *IEEE Trans. Power Electron.*, vol. 37, no. 1, pp. 125–136, Jan. 2022.
- [11] J. Zhao, C. Xie, K. Li, J. Zou, and J. M. Guerrero, "Passivity-oriented design of LCL-type grid-connected inverters with Luenberger observer-based active damping," *IEEE Trans. Power Electron.*, vol. 37, no. 3, pp. 2625–2635, Mar. 2022.
- [12] G. Ma, C. Xie, C. Li, J. Zou, and J. M. Guerrero, "Passivity-based design of passive damping for LCL-type grid-connected inverters to achieve full-frequency passive output admittance," *IEEE Trans. Power Electron.*, vol. 38, no. 12, pp. 16048–16060, Dec. 2023.
- [13] D. G. Photovoltaics and E. Storage, "IEEE standard for interconnection and interoperability of distributed energy resources with associated electric power systems interfaces," IEEE Standard 1547–2018, 2018.
- [14] M. Bajaj and A. K. Singh, "Grid integrated renewable DG systems: A review of power quality challenges and state-of-the-art mitigation techniques," *Int. J. Energy Res.*, vol. 44, no. 1, pp. 26–69, 2020.
- [15] F. Hans, W. Schumacher, S.-F. Chou, and X. Wang, "Design of multifrequency proportional-resonant current controllers for voltage-source converters," *IEEE Trans. Power Electron.*, vol. 35, no. 12, pp. 13573–13589, Dec. 2020.
- [16] T. Ye, N. Dai, C.-S. Lam, M.-C. Wong, and J. M. Guerrero, "Analysis, design, and implementation of a quasi-proportional-resonant controller for a multifunctional capacitive-coupling grid-connected inverter," *IEEE Trans. Ind. Appl.*, vol. 52, no. 5, pp. 4269–4280, Sep/Oct. 2016.
- [17] Z. Xin, X. Wang, P. C. Loh, and F. Blaabjerg, "Grid-current-feedback control for LCL-filtered grid converters with enhanced stability," *IEEE Trans. Power Electron.*, vol. 32, no. 4, pp. 3216–3228, Apr. 2017.
- [18] A. Vidal et al., "Assessment and optimization of the transient response of proportional-resonant current controllers for distributed power generation systems," *IEEE Trans. Ind. Electron.*, vol. 60, no. 4, pp. 1367–1383, Apr. 2013.
- [19] O. Husev, C. Roncero-Clemente, E. Makovenko, S. P. Pimentel, D. Vinnikov, and J. Martins, "Optimization and implementation of the proportional-resonant controller for grid-connected inverter with significant computation delay," *IEEE Trans. Ind. Electron.*, vol. 67, no. 2, pp. 1201–1211, Feb. 2020.
- [20] J. Xu, H. Qian, Y. Hu, S. Bian, and S. Xie, "Overview of SOGI-based single-phase phase-locked loops for grid synchronization under complex grid conditions," *IEEE Access*, vol. 9, pp. 39275–39291, 2021.
- [21] S. Golestan, J. M. Guerrero, M. J. Rawa, A. M. Abusorrah, and Y. Al-Turki, "Frequency-locked loops in electrical power and energy systems: Equivalent or different to phase-locked loops?," *IEEE Ind. Electron. Mag.*, vol. 15, no. 4, pp. 54–64, Dec. 2021.

- [22] B. Shakerighadi, E. Ebrahimzadeh, M. G. Taul, F. Blaabjerg, and C. L. Bak, "Modeling and adaptive design of the SRF-PLL: Nonlinear time-varying framework," *IEEE Access*, vol. 8, pp. 28635–28645, 2020.
- [23] M. Z. Islam, M. S. Reza, M. M. Hossain, and M. Ciobotaru, "Accurate estimation of phase angle for three-phase systems in presence of unbalances and distortions," *IEEE Trans. Instrum. Meas.*, vol. 71, Dec. 2022, Art. no. 9001712.
- [24] W. Xu, C. Huang, and H. Jiang, "Analyses and enhancement of linear Kalman-filter-based phase-locked loop," *IEEE Trans. Instrum. Meas.*, vol. 70, Sep. 2021, Art. no. 6504510.
- [25] W. Xu, C. Huang, and S. Golestan, "Design-oriented study of the orthogonal vector-based linear Kalman filter: Enhancements and applications," *IEEE Trans. Ind. Electron.*, vol. 69, no. 12, pp. 13359–13372, Dec. 2022, doi: [10.1109/TIE.2022.3142415](https://doi.org/10.1109/TIE.2022.3142415).
- [26] H. Ahmed, S. Biricik, and M. Benbouzid, "Linear Kalman filter-based grid synchronization technique: An alternative implementation," *IEEE Trans. Informat.*, vol. 17, no. 6, pp. 3847–3856, Jun. 2021.
- [27] X. Wang, L. Harnefors, and F. Blaabjerg, "Unified impedance model of grid-connected voltage-source converters," *IEEE Trans. Power Electron.*, vol. 33, no. 2, pp. 1775–1787, Feb. 2018.
- [28] S. Golestan, M. Monfared, F. D. Freijedo, and J. M. Guerrero, "Dynamics assessment of advanced single-phase PLL structures," *IEEE Trans. Ind. Electron.*, vol. 60, no. 6, pp. 2167–2177, Jun. 2013.
- [29] A. Kulkarni and V. John, "Analysis of bandwidth–unit-vector-distortion tradeoff in PLL during abnormal grid conditions," *IEEE Trans. Ind. Electron.*, vol. 60, no. 12, pp. 5820–5829, Dec. 2013.
- [30] F. Gonzalez-Espin, G. Garcerá, I. Patrao, and E. Figueres, "An adaptive control system for three-phase photovoltaic inverters working in a polluted and variable frequency electric grid," *IEEE Trans. Power Electron.*, vol. 27, no. 10, pp. 4248–4261, Oct. 2012.
- [31] K.-J. Lee, J.-P. Lee, D. Shin, D.-W. Yoo, and H.-J. Kim, "A novel grid synchronization PLL method based on adaptive low-pass notch filter for grid-connected PCS," *IEEE Trans. Ind. Electron.*, vol. 61, no. 1, pp. 292–301, Jan. 2014.
- [32] A. Tarraso, J. I. Candela, J. Rocabert, Z. Miletic, and A. Luna, "Grid forming control for power converters based on an inertial phase locked loop (IPLL)," *IEEE Access*, vol. 11, pp. 76008–76019, 2023.
- [33] G. Li, Y. Chen, A. Luo, and Y. Wang, "An inertia phase locked loop for suppressing sub-synchronous resonance of renewable energy generation system under weak grid," *IEEE Trans. Power Syst.*, vol. 36, no. 5, pp. 4621–4631, Sep. 2021.
- [34] M. Z. Mansour, M. H. Ravanji, A. Karimi, and B. Bahrani, "Linear parameter-varying control of a power-synchronized grid-following inverter," *IEEE Trans. Emerg. Sel. Topics Power Electron.*, vol. 10, no. 2, pp. 2547–2558, Apr. 2022.
- [35] A. Yazdani and R. Iravani, *DC/AC Half-Bridge Converter*. Hoboken, NJ, USA: Wiley, 2010, pp. 21–47.
- [36] R. W. Erickson and D. Maksimović, "Circuit averaging, averaged switch modeling, and simulation," in *Fundamentals of Power Electronics*. Cham, Switzerland: Springer, 2020, pp. 547–583. [Online]. Available: [https://doi.org/10.1007/978-3-030-43881-4\\_14](https://doi.org/10.1007/978-3-030-43881-4_14)
- [37] A. Yazdani and R. Iravani, *Space Phasors and Two-Dimensional Frames*. Hoboken, NJ, USA: Wiley, 2010, pp. 69–114.
- [38] A. Yazdani and R. Iravani, *Voltage-Sourced Converters in Power Systems: Modeling, Control, and Applications*. Hoboken, NJ, USA: Wiley, 2010.
- [39] A. Yazdani and R. Iravani, *Back-to-Back HVDC Conversion System*. Hoboken, NJ, USA: Wiley, 2010, pp. 334–384.
- [40] P. Rodríguez, J. Pou, J. Bergas, J. I. Candela, R. P. Burgos, and D. Boroyevich, "Decoupled double synchronous reference frame PLL for power converters control," *IEEE Trans. Power Electron.*, vol. 22, no. 2, pp. 584–592, Mar. 2007.
- [41] P. D. Achlerkar and B. K. Panigrahi, "New perspectives on stability of decoupled double synchronous reference frame PLL," *IEEE Trans. Power Electron.*, vol. 37, no. 1, pp. 285–302, Jan. 2022.
- [42] S. Skogestad and I. Postlethwaite, *Multivariable Feedback Control: Analysis and Design*. Hoboken, NJ, USA: Wiley, 2005, pp. 15–62.
- [43] R. Wang, Q. Sun, H. Zhang, L. Liu, Y. Gui, and P. Wang, "Stability-oriented minimum switching/sampling frequency for cyber-physical systems: Grid-connected inverters under weak grid," *IEEE Trans. Circuits Syst. I: Reg. Papers*, vol. 69, no. 2, pp. 946–955, Feb. 2022.
- [44] M. M. Seron, J. H. Braslavsky, and G. C. Goodwin, *SISO Control*. London, U.K.: Springer, 1997, pp. 47–84.



**Alireza Askarian** (Member, IEEE) received the B.Sc. degree in mechanical engineering from the Sharif University of Technology, Tehran, Iran, in 2015. He is currently working toward the Ph.D. degree in application of advanced control algorithms to improve the stability and performance of power electronics with the Department of Mechanical Science and Engineering, University of Illinois at Urbana-Champaign, Urbana, IL, USA.

He is developing a novel microgrid control architecture to meet the reliability, efficiency, and resiliency challenges of the grid system presented by widespread distributed and stochastic renewable power generation. His research focuses on adopting key technologies developed by this research for the future grid system.



**Jaesang Park** (Graduate Student Member, IEEE) received the B.S. and M.S. degrees in mechanical engineering from Yonsei University, Seoul, Korea, in 2014 and 2016 respectively. He is currently working toward the Ph.D. degree in application of advanced control theory to power electronics and power networks with the Department of Mechanical Science and Engineering, University of Illinois at Urbana-Champaign, Urbana, IL, USA.

He is developing a framework for the integration of renewable energy based on the microgrid concept, with a high bandwidth and robust physical layer augmented with an optimized economic layer. His research focuses on the development of a robust and optimal inverter control architecture for microgrid applications.



**Srinivasa Salapaka** (Senior Member, IEEE) received the B.Tech. degree in mechanical engineering from the Indian Institute of Technology, Chennai, India, in 1995, and the MS and Ph.D. degrees in mechanical engineering from the University of California, Santa Barbara, CA, USA, in 1997 and 2002, respectively.

From 2002 to 2004, he was a Postdoctoral Associate with the Laboratory for Information and Decision Systems, Massachusetts Institute of Technology, Cambridge, MA, USA. Since 2004, he has been a Faculty Member with the Department of Mechanical Science and Engineering, University of Illinois at Urbana-Champaign, Urbana, IL, USA. His research interests include controls for nanotechnology, combinatorial resource allocation, and numerical analysis.

Dr. Salapaka was the recipient of the National Science Foundation CAREER Award in 2005.